To the Graduate Council:

I am submitting herewith a thesis written by Jesse M. Labello entitled "Characterization of the Temperature Dependence of Optical Components in a Cryo-Vacuum Chamber used for Space Sensor Testing". I have examined the final paper copy of this thesis for form and content and recommend that it be accepted in partial fulfillment of the requirements for the degree of Master of Science, with a major in Physics.

Dr. Horace W. Crater, Major Professor

We have read this thesis
and recommend its acceptance:

Dr. Lloyd M. Davis

Dr. Christian G. Parigger

Accepted for the Council:

Carolyn R. Hodges, Vice Provost
and Dean of the Graduate School

Characterization of the Temperature Dependence of Optical Components in a Cryo-Vacuum Chamber used for Space Sensor Testing

A Thesis
Submitted for
the Degree of
Master of Science

The University of Tennessee Space Institute,
Tullahoma

Jesse M. Labello
December 2007

Acknowledgments

I am indebted to my family for their support and encouragement. I thank my parents, Donnie and Marie, who always supported me and pushed for a good education. I thank my brothers for, in Nick's (Dr. Labello now) case, giving me someone to look up to and, in Brady's case, someone to be a role model for. I also thank my Grandpa A.J. Schexnayder for many things, but especially for teaching me how to play poker and rummy in the mornings before the school bus came.

I would also like to thank my research advisor, Dr. Heard Lowry, for patience and steadfast support throughout my graduate education. Thanks also to my academic advisor, Dr. Horace Crater for his wisdom on the best way to accomplish my goals in graduate school. I also thank Dr. Christian Parigger who went out of his way on several occasions to lend advice and ideas when I was stuck. I would like to thank Dr. Daniel McCarthy for really making me see what physics is all about and encouraging me to stay with it. I thank everybody who has influenced my education and given me opportunities with special recognition to Dr. Pieter Visscher.

Finally, I'd like to thank all my friends for many things (lengthy discussions about anything imaginable, long nights of playing Halo or cards, etc.), but especially for their sense of humor, pride, and blue collar ethics. Special recognition to Adam Blount, Matthew Martin, and Josh Courtney.

Abstract

The space sensor cryo-vacuum chambers at Arnold Air Force Base are world class sensor characterization and calibration facilities. The chambers provide a simulated deep space background and accurate infrared projections. Several large optical systems are used within the chambers to accomplish this. Calibration of the chambers requires the use of a database of the measured optical properties of these components to simulate the output. However, as the information in the database is room temperature information and the chambers run near 20K, some discrepancies exist between the actual output and the model output. The purpose of this work is to translate the room temperature spectral information to cryogenic information as correctly as possible. To achieve this, the relevant temperature dependent material information was collected from literature. A program was written using this information that calculated spectral performance with temperature as a parameter. An ambient calculation and a cryogenic calculation were performed where necessary for each component of interest. The translation between the two calculations was then measured and applied to the measured ambient data of the components to obtain their expected cryogenic performance.

Contents

1 Introduction **2**

2 Materials **4**
2.1 Dispersion Relations for Modeling of the Refractive Index 4
2.2 Dispersion of Materials of Interest 5
2.2.1 Germanium 5
2.2.2 Magnesium Oxide 6
2.2.3 Thorium Fluoride 7
2.2.4 Zinc Selenide 7
2.2.5 Zinc Sulphide 8

3 Wave Propagation in Multilayers **10**
3.1 Derivation of the Characteristic Matrix 11
3.2 Spectral Profiling of a Homogeneous Dielectric Thin Film Multilayer . 14

4 Chamber Component Analysis **17**
4.1 Beam Combiners Cryogenic Characterization 18
4.2 Bandpass Filters Cryogenic Characterization 25

5 The Chamber Model and Results **34**

6 Conclusion **39**
6.1 Future Research 39

A Derivation of the Characteristic Matrix of a Homogeneous Dielectric Thin Film **44**

B Example Multilayer Calculation **46**
B.1 Calculation Program Results 47

Vita **49**

List of Figures

2.1 Germanium dispersion as given by equation 2.8. 6
2.2 Magnesium oxide dispersion as given by equation 2.9. 7
2.3 Zinc selenide dispersion as given by equation 2.10. 8
2.4 Zinc sulphide dispersion as given by equation 2.11. 9

3.1 An illustration of light propagating through a multilayer. 10
3.2 Notation used for non-absorbing, multilayer calculations. 14

4.1 Block diagram of the cryo-vacuum chamber. 17
4.2 Calculation and measurement of the beam combiners anti-reflection coating. 18
4.3 The design predictions and measurements for the beam combiners supplied by the vendor. 19
4.4 Beam combiner 7 at ambient temperature calculation (red) and measurement (green). 20
4.5 Calculation results for beam combiner 7 at 298K (red) and 20K (blue). 20
4.6 Example measurement of the transmission shift for BC7. 21
4.7 Beam combiner 7 shift application showing the room temperature and new cryogenic spectra. 21
4.8 BC1 (light green) and BC5 (dark green) measurement shown with calculation at 298K (red). 22
4.9 Calculation results for beam combiners 1 and 5 at 298K (red) and 20K (blue). 22
4.10 Example measurement of wavelength shift where the features of the calculation do not align with the measured features for BC1 and BC5. 23
4.11 Example determination of transmission shift in the band of interest where agreement between calculation and measurement is better. . . 23
4.12 Beam combiner-1 spectral data before and after cryo-shift. To the left of the line, $\Delta\lambda$ was applied while the transmission was held constant. Right of the line, the shift was applied through direct addition of $\Delta\mathcal{T}$ while lambda was held constant. 24
4.13 Beam combiner-5 spectral data before and after cryo-shift. To the left of the line, $\Delta\lambda$ was applied while the transmission was held constant. Right of the line, the shift was applied through direct addition of $\Delta\mathcal{T}$ while lambda was held constant. 24
4.14 The measured spectra of the three selected bandpass filters. 26

4.15 The band 1 and band 2 bandpass filters ambient measurements shown with their respective witness measurements at room temperature and 20K. 27
4.16 Example of a wavelength and transmission shift measurement for the band 1 filter witness. 28
4.17 The wavelength shift for the band 1 filter as a function of the ambient wavelength. 28
4.18 The transmission shift for the band 1 filter as a function of the ambient wavelength. 29
4.19 The ambient measurement and the new cryogenic spectrum after applying the measured shifts from the witness. 29
4.20 Example of a wavelength and transmission shift measurement for the band 2 filter witness. 30
4.21 The wavelength shift for the band 2 filter as a function of the ambient wavelength. 30
4.22 The transmission shift for the band 2 filter as a function of the ambient wavelength. 31
4.23 The ambient measurement and the new cryogenic spectrum after applying the measured shifts from the witness. 31
4.24 The ambient measurement and the new cryogenic spectrum after applying the averaged shifts. 32
4.25 The calculation results for the Software Spectra, Inc. wide bandpass filter prescription using constant refractive indices (a) from FreeSnell, and (b) from the calculation program. 33
4.26 The calculation results for the Software Spectra, Inc. wide bandpass filter prescription using the temperature dependent dispersion relations from section 1.2 for germanium and zinc sulphide. 33

5.1 Diagram of the measured radiation paths. 34
5.2 Blackbody curves highlighting the 6-l2 μm range. 35
5.3 The throughput of blackbody 1 at 400K before (red) and after (blue) cryo-shifting of the selected components shown with measurement. . . 36
5.4 The throughput of blackbody 1 at 700K, model and measurement results. Point 3 is the band 1 filter. Point 4 is the band 2 filter. Point 5 is the band 1+2 filter. 36
5.5 The throughput of blackbody 2 at 400K before (red) and after (blue) cryo-shifting of the selected components shown with measurement. . . 37
5.6 The throughput of blackbody 2 at 700K, model and measurement results. Point 3 is the band 1 filter. Point 4 is the band 2 filter. Point 5 is the band 1+2 filter. 37
5.7 A before and after comparison of the 10V model. The left chart shows the absolute value percent difference between test data and model prediction with the blackbodies at 400K. The right chart shows the same with blackbodies at 700K. 38

B.1 Prescription for a cold mirror designed to reflect shorter wavelengths and transmit longer ones, courtesy of Software Spectra, Inc [SSI, 2007]. 46
B.2 (a) The results from FreeSnell. (b) The results from the calculation program. 48

Chapter 1

Introduction

The test facility under consideration for this work is a large cryo-vacuum chamber designed to test high performance interceptor and surveillance sensors. The chamber is 10 feet in diameter and about 30 feet long. To isolate vibrations it is structurally anchored to a 300,000lb seismic mass. Helium shrouds allow for operating temperatures around 20K at a vacuum of 10^{-6}Torr. To complement the physical structure of the chamber, the systems inside are composed of high quality optics and sources that include blackbodies and resistor arrays. The different systems are utilized and combined to provide infrared scenes with accurate background and target information for the sensor under test. For proper testing of such sensitive sensors to be assured, the chamber must be calibrated exactly. To this end, the computer model of the chamber is used. This places a high priority on the integrity of the computer model [Lowry et al., 2004b].

Only within the past decade have serious efforts been put forth to catalogue the effect of temperature on optical coefficients. The reason for that is most likely that the temperature effect is relatively small and has not been previously deemed worth the effort it takes to measure. However, many people in the space simulation community, and infrared community in general, find that they cannot ignore temperature effects and with today's better technology these effects are more commonly being taken into account. The result of thermal characterization of an optical material is generally a temperature dependent dispersion relation for the refractive index. The extinction coefficient and/or absorption characteristics may have also been characterized depending on several factors including motive, material, and wavelength range of interest. In the field of infrared transmitting materials, Hawkins *et al* at the University of Reading may very well have done the largest amount of work on temperature dependence with thorough characterizations of many materials and whole optical components over wide wavelength and temperature ranges [IML, 2007].

In general, optical materials are characterized by transmitting regions where the extinction coefficient of the material is almost universally negligible. Mid-infrared optical materials generally have their primary transmitting regions in between $2\mu m$ and about $15\mu m$. The transmitting region is bounded by areas of absorption with corresponding rises in the extinction coefficient. Electronic absorption, responsible for the short wavelength cutoff, is caused by the incident radiation exciting electrons

or holes in the material. Lattice absorption is responsible for the long wavelength cutoff and occurs because the incident radiation couples with phonons in the crystal [Hawkins, 1998].

Optical components are typically designed to be used within their materials' primary transmitting regions. The effects of temperature on a multilayer component are easily identified. The refractive index, the extinction coefficient, and the thermal expansion of materials are all functions of temperature to some degree. However, if the wavelength region of interest is restricted to only the material's primary transmitting regions, the extinction coefficient may generally be ignored as it is negligible in that region. Also, when dealing with thin film layers of micron to nanometer scale, the thermal expansion may also be ignored. Therefore, to characterize the effect of temperature on a multilayer to good approximation within the wavelength range it was designed for, all that is needed is the temperature dependence of the refractive index of its composite materials.

Chapter 2

Materials

2.1 Dispersion Relations for Modeling of the Refractive Index

In regions where there are no resonant frequencies, it is possible, and practical, to use empirical relations to adequately describe the dispersion of the refractive index of a material. There are several popular equations that are fit to data and then used in this manner across a wide wavelength range. Some of the more common ones are:

- Cauchy's

$$n(\lambda) = A_n + \frac{B_n}{\lambda^2} + \frac{C_n}{\lambda^4} + \dots \tag{2.1}$$

$$k(\lambda) = A_k + \frac{B_k}{\lambda^2} + \frac{C_k}{\lambda^4} + \dots \tag{2.2}$$

  These are empirical equations that are usually only valid for normal dispersion in the visible region. The coefficients A, B, C, and so on are fitting parameters [Poelman and Smet, 2003].

- Sellmeier's

$$n(\lambda) = \sqrt{A + \frac{B\lambda^2}{\lambda^2 - C} + \frac{D\lambda^2}{\lambda^2 - E}} \tag{2.3}$$

$$k(\lambda) = \frac{1}{n(\lambda)(D_1\lambda + \frac{D_2}{\lambda} + \frac{D_3}{\lambda^3})} \tag{2.4}$$

  Sellmeier's equation is based on Cauchy's formula. These empirical relations are typically used for the infrared region although their validity can extend into the visible and even ultraviolet in some instances. The three term Sellmeier equation for $n(\lambda)$ shown is the most common in use. The coefficients A, B, C, D, E, and $D_{1,2,3}$ are fitting parameters [Poelman and Smet, 2003].

- Buchdahl's

$$n(\lambda) = A + B\lambda + C\lambda^2 + D\lambda^3 + \ldots \tag{2.5}$$

Buchdahl's empirical polynomial is based on his dispersion theory. A, B, C, D, and so on are fitting parameters [Robb and Mercado, 1983].

- Forouhi-Bloomer's

$$n(E) = n(\infty) + \sum_{i}^{q} \frac{B_{0i}E + C_{0i}}{E^2 - B_iE + C_i} \tag{2.6}$$

$$k(E) = \sum_{i=1}^{q} \frac{A_i(E - E_g)^2}{E^2 - B_iE + C_i} \tag{2.7}$$

E is photon energy so that $E = \frac{hc}{\lambda}$. E_g is the band gap of the material. A, B, and C are coefficients related to the electronic structure of the material. B_0 and C_0 depend upon E_g, A, B, and C. Published in 1986, FB's equations are not empirical in nature as they were derived from first principles. They are valid from deep ultraviolet to the near infrared [Poelman and Smet, 2003].

The Forouhi-Bloomer equations would be the preferred choice in putting together a physical model to describe multilayer optics, however, the selection of materials characterized by these equations was found to be limited. So, for this work, the commonly used Sellmeier's expression and the simple Buchdahl's polynomial will be used primarily. Using these expressions as the wavelength dependence and allowing the fitting parameters to become functions of temperature gives a model of $n(\lambda, T)$.

2.2 Dispersion of Materials of Interest

2.2.1 Germanium

Germanium is a group IV semiconductor with good mechanical properties and a high refractive index, ($n \approx 4$), making it ideal for many optical applications. Its main transmission region is $2 - 20\mu m$. Barnes and Piltch [Barnes and Piltch, 1979] published the following temperature dependent Sellmeier expression for germanium that holds well over the entire primary transmission region [Hawkins, 1998, Icenogle et al., 1976].

$$n_{Ge}(\lambda, T) = \sqrt{A(T) + \frac{B(T)\lambda^2}{\lambda^2 - C(T)} + \frac{D(T)\lambda^2}{\lambda^2 - E(T)}} \tag{2.8}$$

$$\begin{aligned} A(T) &= -6.040 * 10^{-3}\ T + 11.05128 \\ B(T) &= 9.295 * 10^{-3}\ T + 4.00536 \\ C(T) &= -5.392 * 10^{-4}\ T + 0.599034 \\ D(T) &= 4.151 * 10^{-4}\ T + 0.09145 \\ E(T) &= 1.51408\ T + 3426.5 \end{aligned}$$

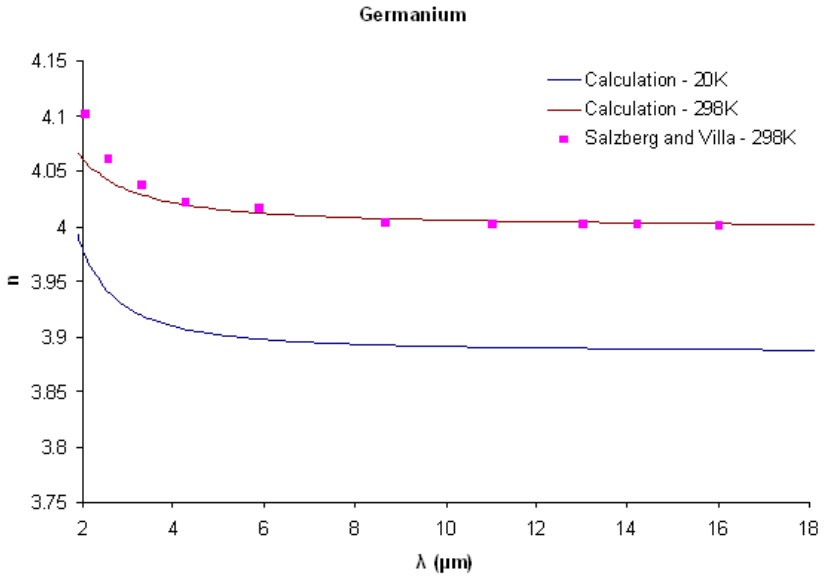


Figure 2.1: Germanium dispersion as given by equation 2.8.

In the early 1970's, A.J. Moses [Moses, 1970] put together a report containing measured data from literature on many infrared materials. Salzberg and Villa's [Salzberg and Villa, 1958] data for single crystal germanium was extracted from Moses' report for comparison with the dispersion relation here (see figure 2.1). Germanium does not display much wavelength dependence over it's primary transmission region, but the temperature effect is well pronounced as the refractive index drops with lowered temperature.

2.2.2 Magnesium Oxide

Magnesium oxide is a naturally occurring compound with a multitude of industrial uses. As an optical material it has a primary transmission region of one to six microns. Stephens and Malitson [Stephens and Malitson, 1952] originally found a dispersion relation at ambient temperatures. Using that and the reported $\frac{dn}{dT}$ of $19 * 10^{-6}/K$ at 298K the following temperature dependent polynomial was found to hold well over the primary transmission region at room temperature:

$$n_{MgO}(\lambda, T) = A(T) + B(T)\lambda + C(T)\lambda^2 + D(T)\lambda^3 \tag{2.9}$$

$$\begin{aligned} A(T) &= 1.86691 * 10^{-5}\ T + 1.74722 \\ B(T) &= -3.59712 * 10^{-10}\ T - 2.62452 * 10^{-2} \\ C(T) &= 7.19424 * 10^{-11}\ T + 3.12036 * 10^{-3} \\ D(T) &= -3.59712 * 10^{-12}\ T - 5.06512 * 10^{-4} \end{aligned}$$

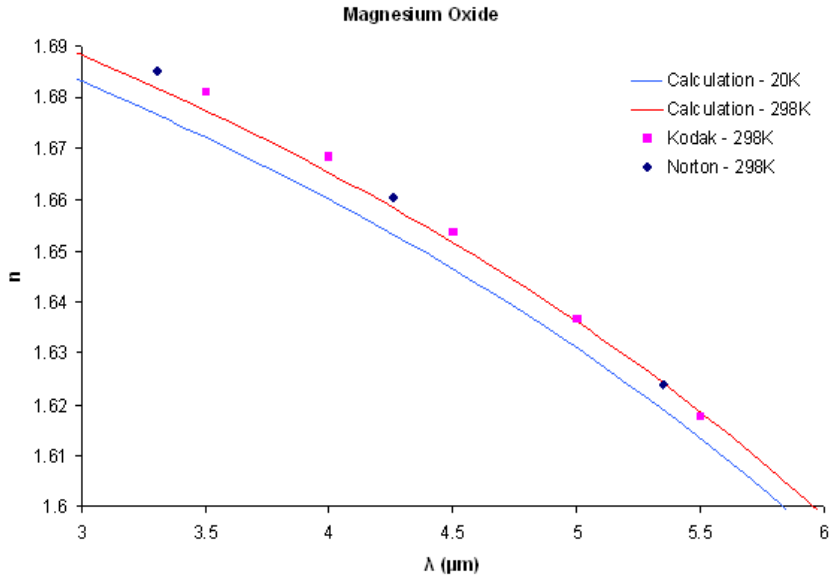


Figure 2.2: Magnesium oxide dispersion as given by equation 2.9.

Norton Co. performed measurements on bulk, single crystal magnesium oxide [Norton, 1962] and Kodak measured the refractive index of bulk, polycrystalline MgO [Kodak, 1967]. Their data was extracted from Moses' report for comparison here (see figure 2.2) [Moses, 1970]. The temperature data on magnesium oxide was found to be quite limited, which is why the polynomial was obtained using the constant $\frac{dn}{dT}$ at 298K. However, it does not display much temperature dependence even using this constant $\frac{dn}{dT}$, which actually decreases slightly with temperature, which is quite likely why the data is limited.

2.2.3 Thorium Fluoride

Thorium fluoride is a very low refractive index material used primarily in anti-reflection coatings in the mid-infrared. It is a naturally radioactive material that requires special handling precautions, however, its benefits of good adhesion, low index, and decent mechanical properties mean that it is still used often in high quality optics. ThF_4 has a primary transmission region of about $0.25 - 10.5\mu m$. Perhaps due to its radioactive nature, no temperature data was found on this material and, as a result, a constant 1.40 was used for the refractive index in the calculations [Palik, 1991].

2.2.4 Zinc Selenide

Zinc selenide is an intrinsic semiconductor with a mid-range refractive index (≈ 2.4). The primary transmission window is $3 - 15\mu m$. Marple [Marple, 1964] originally found a Sellmeier type expression for it. Hawkins elaborated upon the work to find

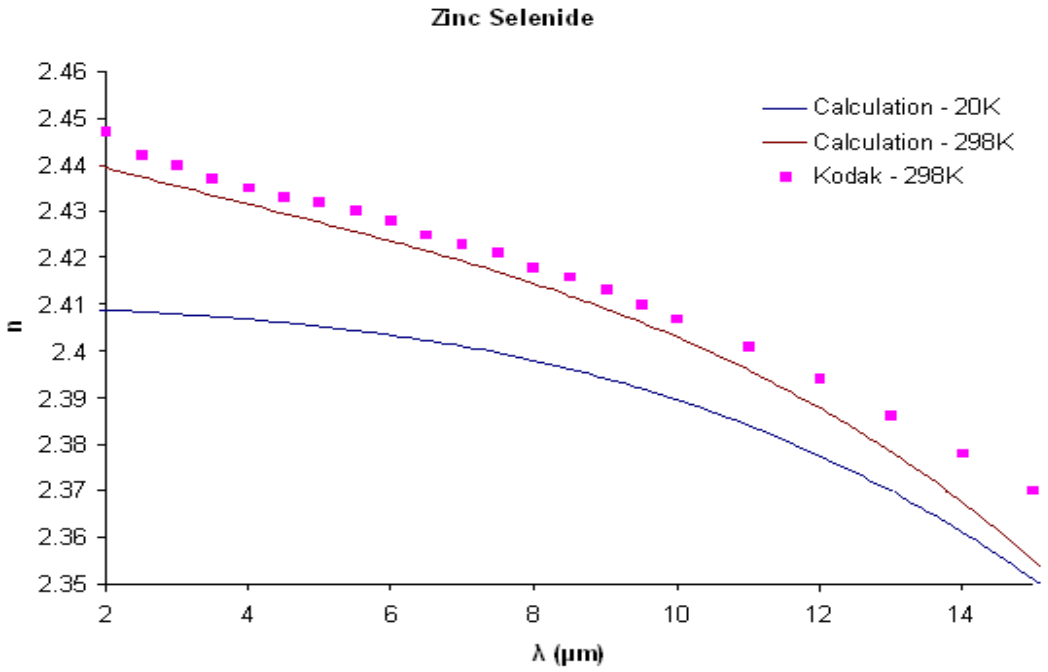


Figure 2.3: Zinc selenide dispersion as given by equation 2.10.

the following temperature dependent dispersion equation which holds well over the primary transmission region [Hawkins, 1998]:

$$n_{ZnSe}(\lambda, T) = A(T) + B(T)\lambda + C(T)\lambda^2 + D(T)\lambda^3 \tag{2.10}$$

$$\begin{aligned} A(T) &= 1.509 * 10^{-4}\ T + 2.407 \\ B(T) &= -1.801 * 10^{-5}\ T - 2.564 * 10^{-4} \\ C(T) &= 1.300 * 10^{-6}\ T - 1.308 * 10^{-5} \\ D(T) &= -3.878 * 10^{-8}\ T - 1.480 * 10^{-5} \end{aligned}$$

Kodak performed measurements on bulk, polycrystalline ZnSe which was extracted from Moses' report for comparison here (see figure 2.3) [Kodak, 1967, Moses, 1970]. Zinc selenide displays a fairly large wavelength dependence and a temperature dependence that is well pronounced at shorter wavelengths and decreases over the primary transmission band.

2.2.5 Zinc Sulphide

Zinc sulphide is a naturally occurring yellowish compound that is hot pressed into what is known as Cleartran®. The primary transmission region is about $0.4 - 10\mu m$. Feldman [Feldman et al., 1978] found a polynomial to describe the room temperature dispersion. Hawkins elaborated upon the work to find the following temperature

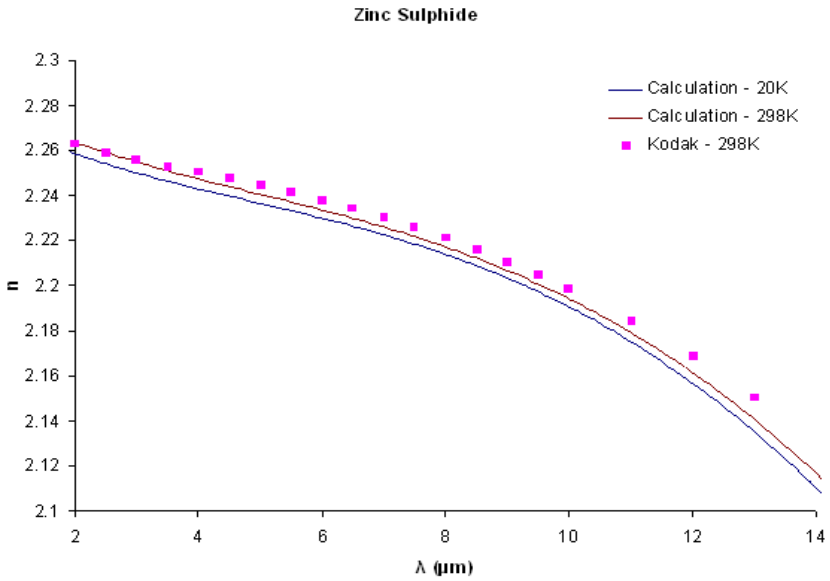


Figure 2.4: Zinc sulphide dispersion as given by equation 2.11.

dependent dispersion relation with good agreement to measurements reported in the $2 - 14\mu m$ range [Hawkins, 1998]:

$$n_{ZnS}(\lambda, T) = A(T) + B(T)\lambda + C(T)\lambda^2 + D(T)\lambda^3 + E(T)\lambda^4 \qquad (2.11)$$

$$\begin{aligned} A(T) &= 5.608 * 10^{-5}\ T + 2.282 \\ B(T) &= -8.671 * 10^{-6}\ T - 1.563 * 10^{-2} \\ C(T) &= 5.549 * 10^{-7}\ T + 2.067 * 10^{-3} \\ D(T) &= 2.597 * 10^{-8}\ T - 1.714 * 10^{-4} \\ E(T) &= -9.798 * 10^{-10}\ T + 2.884 * 10^{-6} \end{aligned}$$

Kodak performed measurements on bulk, polycrystalline ZnS which was extracted from Moses' report for comparison here (see figure 2.4) [Kodak, 1967, Moses, 1970]. Zinc sulphide displays a pronounced wavelength dependence, but very little temperature dependence as the refractive index shows a drop of only about a hundredth from room temperature to 20K over the primary transmission region.

Chapter 3

Wave Propagation in Multilayers

Multilayers are stacks of thin films of nanometer scale that are layered upon a substrate to produce an optical component with the desired properties (see figure 3.1). Those properties might include polarization, anti-reflection, high reflection, a fifty to fifty reflection - to - transmission ratio or just about any other ratio desired. Multilayers work by manipulating the interference from the reflected or transmitted rays. For instance, if an anti-reflection coating is desired, one would maximize the destructive interference of the reflected rays, thereby reducing the reflection and increasing the transmission. The characteristic matrix method is often used to analyze the performance of multilayers. Born and Wolf, [Born and Wolf, 1964], offers a good, fundamental, description of this method which will be outlined in this chapter.

There are several different notations used in optics to describe the fundamental quantities of interest. The notation used here will follow that of Born and Wolf.

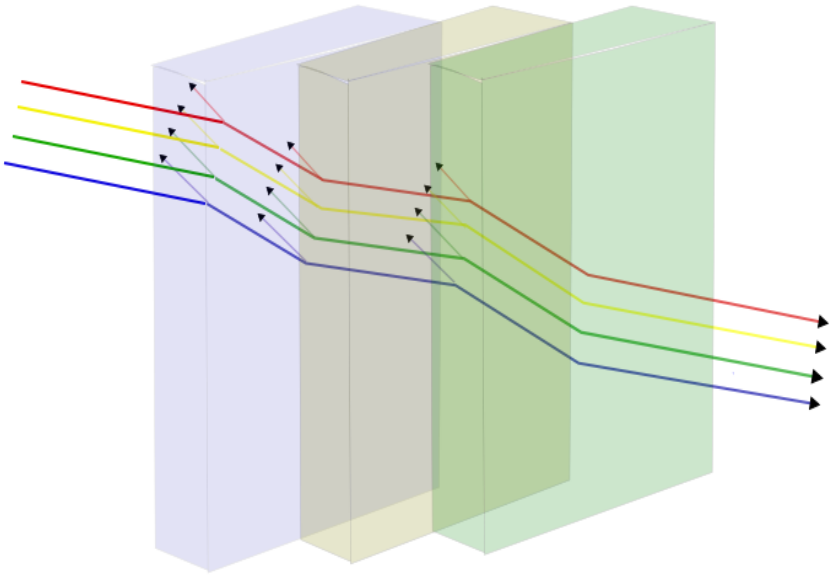


Figure 3.1: An illustration of light propagating through a multilayer.

Polarization of an electromagnetic wave is described as transverse electric, TE, or transverse magnetic, TM. TE describes the special case of linear polarization with the electric vector perpendicular to the plane of incidence and the magnetic vector parallel, this is often called s polarization in other notation. Likewise, TM has the magnetic vector perpendicular to the plane of incidence and the electric vector parallel, also called p polarization elsewhere. The electric field component will be denoted by $\mathbf{E}$. The magnetic component will be handled in terms of the magnetic vector, $\mathbf{H}$, where $\mathbf{H} = (1/\mu)\,\mathbf{B}$ in an isotropic medium and $\mathbf{B}$ is the magnetic induction. Material properties are, standardly, described by the magnetic permeability, μ, and the permittivity, ϵ, which is also often referred to as the dielectric constant.

3.1 Derivation of the Characteristic Matrix

Consider a TE wave incident upon a stratified medium such that $\mu = \mu(z)$ and $\epsilon = \epsilon(z)$. Maxwell's equations are

$$\begin{aligned}
\frac{\partial H_z}{\partial y} - \frac{\partial H_y}{\partial z} + \frac{i\epsilon\omega}{c}E_x = 0 \quad \text{(a)} \qquad & \frac{i\omega\mu}{c}H_x = 0 \quad \text{(d)} \\
\frac{\partial H_y}{\partial z} - \frac{\partial H_z}{\partial x} = 0 \quad \text{(b)} \qquad & \frac{\partial E_x}{\partial z} - \frac{i\omega\mu}{c}H_y = 0 \quad \text{(e)} \\
\frac{\partial H_y}{\partial x} - \frac{\partial H_x}{\partial y} = 0 \quad \text{(c)} \qquad & \frac{\partial E_x}{\partial y} + \frac{i\omega\mu}{c}H_z = 0 \quad \text{(f)},
\end{aligned} \tag{3.1}$$

where ω is the angular frequency of the incident radiation and c is the speed of light in a vacuum.

Inserting 3.1e and 3.1f into 3.1a yields

$$\frac{\partial^2 E_x}{\partial y^2} + \frac{\partial^2 E_x}{\partial z^2} + n^2 k_0^2 E_x = \frac{\partial \ln\mu}{\partial z}\frac{\partial E_x}{\partial z}, \tag{3.2}$$

where n and k_0 are defined by

$$n \equiv \sqrt{\epsilon\mu}, \tag{3.3}$$

$$k_0 \equiv \frac{\omega}{c}\ . \tag{3.4}$$

Separation of variables yields

$$\frac{1}{Y(y)}\frac{\partial^2 Y(y)}{\partial y^2} = -K^2, \tag{3.5}$$

$$-\frac{1}{Z(z)}\frac{\partial^2 Z}{\partial Z^2} - n^2 k_0^2 + (\frac{\partial \ln\mu}{\partial z})\frac{1}{Z(z)}\frac{\partial Z(z)}{\partial z} = -K^2, \tag{3.6}$$

where K is a constant. Letting $K = k_0\alpha$ and assuming a time dependence of $e^{-i\omega t}$, $Y(y)$ has the solution

$$Y(y) = Y_0 e^{i(k_o \alpha y - \omega t)}. \tag{3.7}$$

Therefore E_x is

$$E_x = Z(z) e^{i(k_0 \alpha y - \omega t)}. \tag{3.8}$$

Now, looking at 3.1b and 3.1c it is obvious that

$$H_y = V(z) e^{i(k_0 \alpha y - \omega t)}, \tag{3.9}$$

$$H_z = W(z) e^{i(k_0 \alpha y - \omega t)}. \tag{3.10}$$

Inserting 3.8, 3.9, and 3.10 into 3.1a yields

$$\frac{\partial V(z)}{\partial z} = ik_0[\alpha W(z) + \epsilon Z(z)], \tag{3.11}$$

$$\frac{\partial Z(z)}{\partial z} = ik_0 \mu V(z), \tag{3.12}$$

$$\alpha Z(z) + \mu W(z) = 0. \tag{3.13}$$

3.13 into 3.11 yields

$$\frac{\partial V(z)}{\partial z} = ik_0(\epsilon - \frac{\alpha^2}{\mu}) Z(z). \tag{3.14}$$

Now, 3.12 and 3.14 are a pair of coupled, first-order differential equations for Z(z) and V(z). From these, the second order differential equations in $V(z)$ and $Z(z)$ are

$$\frac{\partial^2 V(z)}{\partial z^2} - \frac{\partial \ln(\epsilon - \frac{\alpha^2}{\mu})}{\partial z} \frac{\partial V(z)}{\partial z} + (n^2 - \alpha^2) k_0^2 V(z) = 0, \tag{3.15}$$

$$\frac{\partial^2 Z(z)}{\partial z^2} - \frac{\partial \ln \mu}{\partial z} \frac{\partial Z(z)}{\partial z} + (n^2 - \alpha^2) k_0^2 Z(z) = 0. \tag{3.16}$$

$V(z)$ and $Z(z)$ may be expressed as a linear combination of two particular solutions that must be coupled by 3.12 and 3.14. If V_1, V_2, Z_1, and Z_2 are solutions to 3.15 and 3.16 respectively, we have

$$Z_1' = ik_0 \mu V_1, \qquad Z_2' = ik_0 \mu V_2,$$

$$V_1' = ik_0(\epsilon - \tfrac{\alpha^2}{\mu}) Z_1, \quad V_2' = ik_0(\epsilon - \tfrac{\alpha^2}{\mu}) Z_2.$$

It follows that

$$V_1 Z_2' - Z_1' V_2 = 0, \tag{3.17}$$

$$Z_1 V_2' - V_1' Z_2 = 0, \tag{3.18}$$

which means,

$$\mathcal{D} = \begin{vmatrix} Z_1 & V_1 \\ Z_2 & V_2 \end{vmatrix} = constant. \tag{3.19}$$

Now choosing

$$Z_1 = f(z), \quad Z_2 = F(z),$$

$$V_1 = g(z), \quad V_2 = G(z),$$

$$\begin{aligned} f(0) &= G(0) = 0, \\ F(0) &= g(0) = 1, \\ Z(0) &\equiv Z_0, \\ V(0) &\equiv V_0, \end{aligned}$$

the solutions may be expressed as

$$Z(z) = Z_0 F(z) + V_0 f(z), \tag{3.20}$$

$$V(z) = Z_0 G(z) + V_0 g(z). \tag{3.21}$$

In matrix notation this becomes,

$$\mathcal{Q} = \mathcal{N}\mathcal{Q}_0, \tag{3.22}$$

$$\mathcal{Q} = \begin{pmatrix} Z(z) \\ V(z) \end{pmatrix}, \tag{3.23}$$

$$\mathcal{Q}_0 = \begin{pmatrix} Z_0 \\ V_0 \end{pmatrix}, \tag{3.24}$$

$$\mathcal{N} = \begin{pmatrix} F(z) & f(z) \\ G(z) & g(z) \end{pmatrix}. \tag{3.25}$$

Now solving for $\mathcal{Q}_0$ yields

$$\mathcal{Q}_0 = \mathcal{M}\mathcal{Q}, \tag{3.26}$$

$$\mathcal{M} = \begin{pmatrix} g(z) & -f(z) \\ -G(z) & F(z) \end{pmatrix}. \tag{3.27}$$

$\mathcal{M}$ is called the *characteristic matrix* of the medium. It relates the components of the field vectors at some plane z to the components at the plane $z = 0$ [Born and Wolf, 1964].

3.2 Spectral Profiling of a Homogeneous Dielectric Thin Film Multilayer

The characteristic matrix for a TE wave in a stratified dielectric medium is derived in Appendix A. It is

$$M_j = \begin{pmatrix} \cos\delta_j & -\frac{i}{p_j}\sin\delta_j \\ -ip_j\sin\delta_j & \cos\delta_j \end{pmatrix}, \tag{3.28}$$

$$\delta_j = \frac{2\pi n_j t_j}{\lambda}\cos\theta_j, \tag{3.29}$$

$$p_j = \sqrt{\frac{\epsilon_j}{\mu_j}}\cos\theta_j, \tag{3.30}$$

where n is the refractive index defined by equation 3.3 and θ is found by Snell's Law:

$$n_1\sin\theta_1 = n_2\sin\theta_2.$$

The characteristic matrix of multiple layers can be found through the matrix product of the individual layers in order from the incident layer to the exit layer. Using the notation in Figure 3.2, the characteristic matrix of the entire incident side would be

$$M_{inc} = \prod_{j=m}^{0} M_j, \tag{3.31}$$

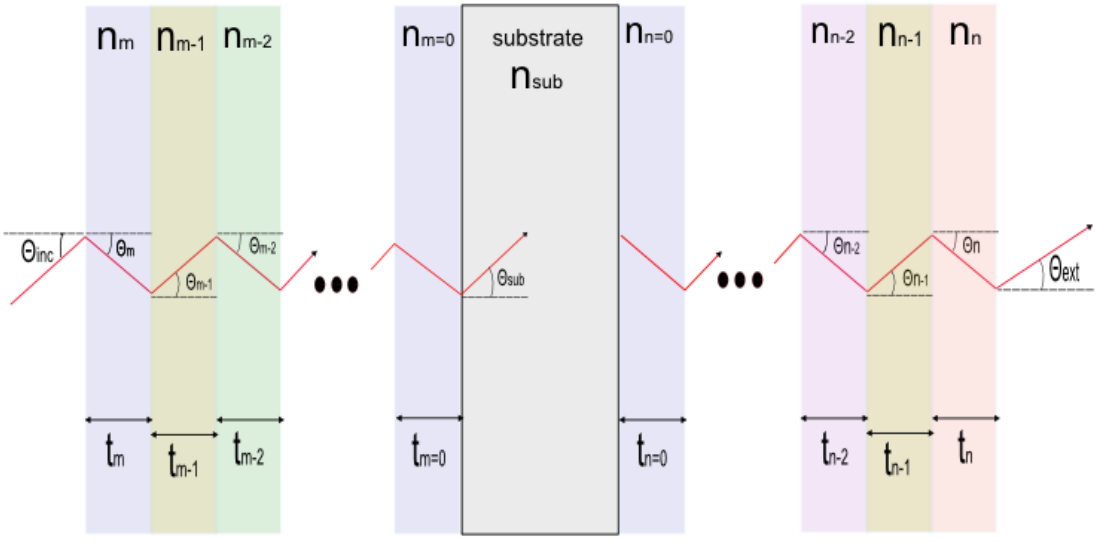


Figure 3.2: Notation used for non-absorbing, multilayer calculations.

and the exit side would be

$$M_{ext} = \prod_{j=0}^{n} M_j. \tag{3.32}$$

Once the characteristic matrix of each side has been found, the transmission and reflection coefficients are given by

$$r = \frac{(m_{11} + m_{12}p_l)p_1 - (m_{21} + m_{22}p_l)}{(m_{11} + m_{12}p_l)p_1 + (m_{21} + m_{22}p_l)}, \tag{3.33}$$

$$t = \frac{2p_1}{(m_{11} + m_{12}p_l)p_1 + (m_{21} + m_{22}p_l)}, \tag{3.34}$$

$$\mathcal{R} = |r|^2, \tag{3.35}$$

$$\mathcal{T} = \frac{p_l}{p_1}|t|^2, \tag{3.36}$$

where the m_{ij}'s are the individual elements of the characteristic matrix of the side. p_l refers to the p of the last, exit, medium and p_1 refers to the first, incident, medium.

The transmission and reflection of the entire double sided element would be

$$\mathcal{T}_{tot} = \mathcal{T}_{inc} \times \mathcal{T}_{ext} \tag{3.37}$$

$$\mathcal{R}_{tot} = \mathcal{R}_{inc} + \mathcal{T}_{inc} \times \mathcal{R}_{ext} \tag{3.38}$$

The process is identical for a TM wave, all that is necessary is to replace p by q where

$$q_j = \sqrt{\frac{\mu_j}{\epsilon_j}} \cos\theta_j. \tag{3.39}$$

For unpolarized radiation, it is necessary to calculate the transmission and reflection coefficients using the p's and the q's separately and then find the average by [Born and Wolf, 1964]

$$\mathcal{R} = \frac{\mathcal{R}_p + \mathcal{R}_q}{2}, \tag{3.40}$$

$$\mathcal{T} = \frac{\mathcal{T}_p + \mathcal{T}_q}{2}. \tag{3.41}$$

Layer absorption can be accounted for by letting n be replaced by the complex index of refraction

$$N = n + ik. \tag{3.42}$$

k is called the extinction coefficient and is related to n through a Hilbert transform called Kramers-Kronig relationship

$$\Im(N^2(\omega) - 1) = \frac{-2}{\pi}\,\mathbf{P}\int_0^\infty \frac{\omega\,\Re(N^2(\omega') - 1)}{\omega'^2 - \omega^2} d\omega', \tag{3.43}$$

$$\Re(N^2(\omega) - 1) = \frac{2}{\pi}\,\mathbf{P}\int_0^\infty \frac{\omega\,\Im(N^2(\omega') - 1)}{\omega'^2 - \omega^2} d\omega'. \tag{3.44}$$

P represents Cauchy's principal value. Thus, the real part of the complex refractive index, n, is specified by knowledge of the imaginary part, k, over all frequencies and vice versa.

The absorption effect can be seen by substituting 3.42 into a plane wave, $e^{i(\kappa x - \omega t)}$. κ is the wave number such that

$$\kappa = \frac{\omega N}{c}. \tag{3.45}$$

Upon insertion, the plane wave becomes

$$e^{i(\kappa x - \omega t)} = e^{i\frac{\omega x}{c}n}\; e^{-\frac{\omega x}{c}k}\; e^{-i\omega t}. \tag{3.46}$$

The middle term is seen to have a damping, or absorptive, effect on the wave function [Arfken and Weber, 2001].

Chapter 4

Chamber Component Analysis

The optical components of the cryo-vacuum chamber that were selected for direct scrutiny consist of three beam combiners and three wide bandpass filters. Two of the beam combiners, BC1 and BC5, were designed to be identical 50/50 components in the 6-12μm band. The other beam combiner, BC7, is a dichroic beam combiner in that it transmits the 6-12μm band through and also reflects a visible band from the other side (see figure 4.1). The bandpass filters were designed to transmit certain mid-infrared bands that are denoted by band 1, band 2, and band 1+2. They are used in the radiation calibration monitoring sytem (RCMS) which uses a computer model to calibrate the chamber [Lowry et al., 2004a]. These components were selected due to their impact on the radiation and in an effort to provide the model, and

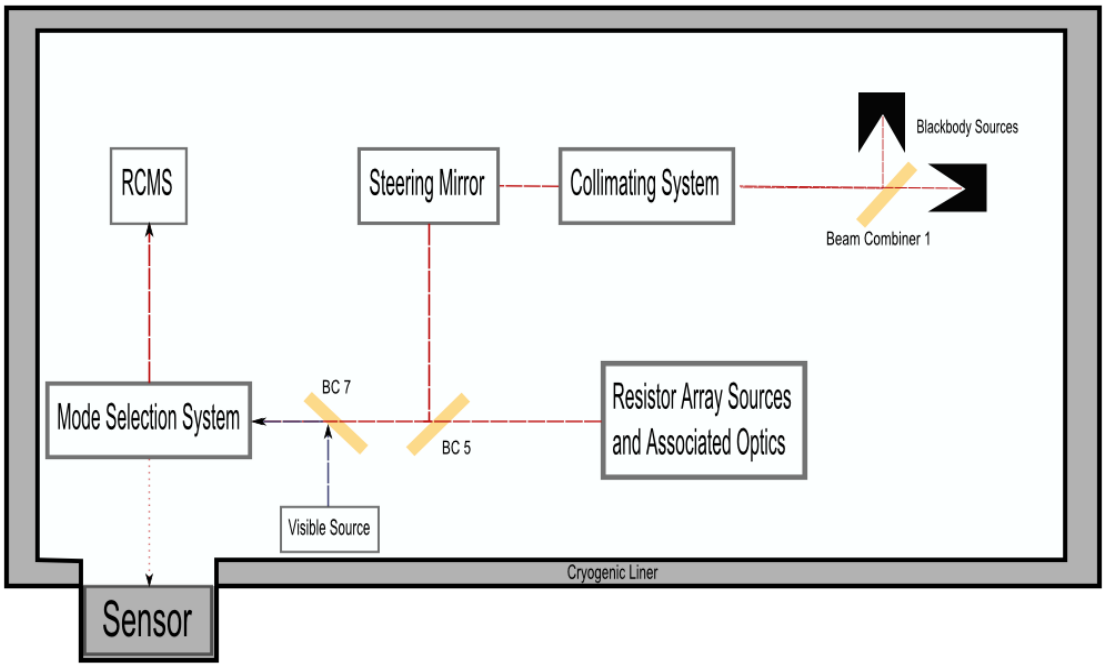


Figure 4.1: Block diagram of the cryo-vacuum chamber.

hence the calibration unit, with the best data possible. To achieve the translation a computer program was coded that uses the multilayer theory and temperature dependent refractive index dispersion relations outlined in the previous sections. The program takes the temperature, angle of incidence, wavelength range desired, and coating prescription as input. It then computes the transmission and reflection in small steps across the wavelength range specified.

4.1 Beam Combiners Cryogenic Characterization

The beam combiners are double sided elements in that they have coatings applied to both sides of the substrate. On the incident side is an anti-reflection coating designed to transmit the 6-12μm range. Outside of this range, especially on the shorter wavelength side, the reflection quickly rises (figure 4.2). On the exit side of the substrate is the actual beam combiner coating that accomplishes the design specifications.

The design prescriptions of the beam combiners were used to calculate their theoretical transmission and reflection at room temperature and at $20K$. The design prescriptions include the material and thickness that each layer is supposed to be. However, the coating process, especially for complex multilayers containing several different materials with each layer being a different thickness, is difficult and inexact. Continuous monitoring during the manufacturing of these elements is necessary, but is not always enough to ensure success as minute changes in conditions can lead to deposition errors. Layers that are fractions of a wavelength off can lead to unpredictable

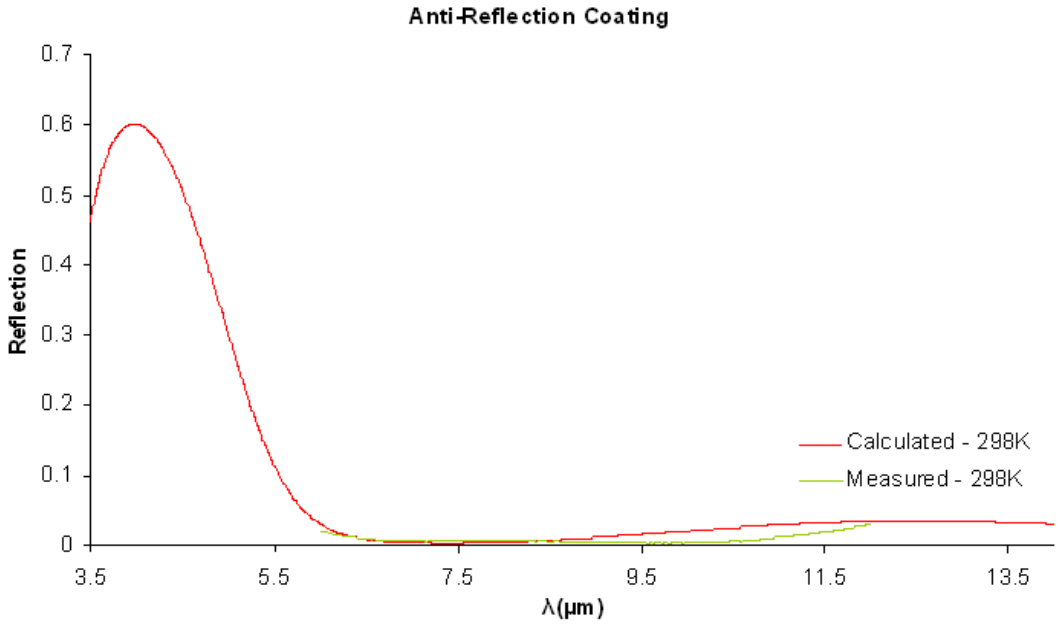


Figure 4.2: Calculation and measurement of the beam combiners anti-reflection coating.

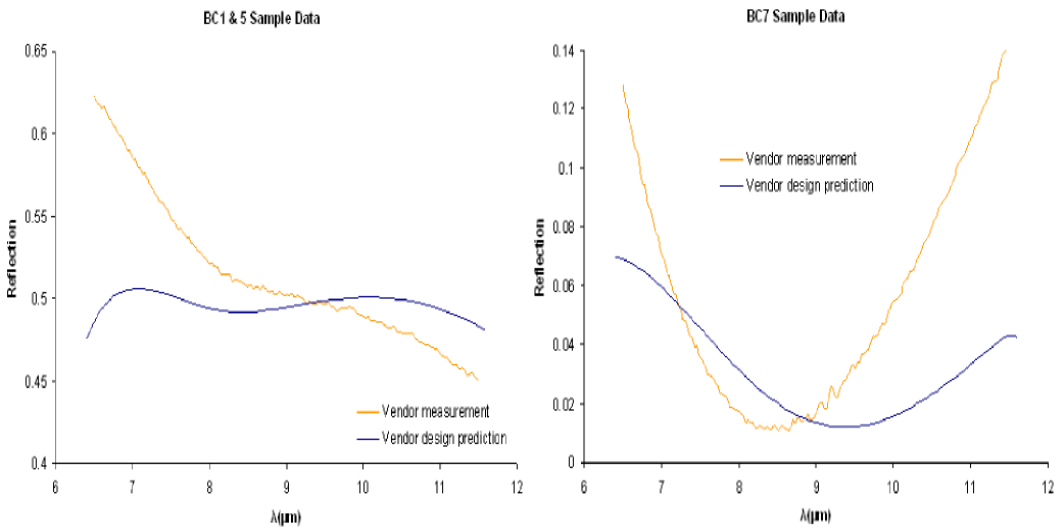


Figure 4.3: The design predictions and measurements for the beam combiners supplied by the vendor.

and, likely, undesired characteristics in the element [Sullivan and Dobrowolski, 1992]. The thicknesses of the individual layers of these beam combiners may be notably different than what they were supposed to be according to the design prescriptions. To illustrate this, the vendor of the beam combiners supplied predictions on these same design prescriptions that did not match very well with the measured data (figure 4.3). However, the agreement between the calculation and measurement at room temperature was fairly good within the spectral band of interest. Outside of the 6-12μm band, the agreement tended to diverge as absorption began to occur and the empirical equations for refractive index were taken out of their useful wavelength range. Comparison of the two calculations show a small shift of features to shorter wavelengths and an increase in transmission with a corresponding decrease in reflection. The shift between the 298K and 20K calculations was measured and applied to the room temperature data to yield a cryogenic spectra for each beam combiner which could then be put into the radiometric computer model (see figures 4.4 - 4.13).

The application was performed in two ways. In areas where the agreement between calculation and measurement was good, the room temperature calculated spectrum was subtracted from the cryogenic calculated spectrum. The difference was then added to the measured spectrum. This method was used for BC7's entire spectrum and part of BC1 and BC5's spectra. Where the agreement was not so good, (*i.e.* features occurring at slightly different wavelengths), in the other part of BC1 and BC5's spectra, the wavelength shift was measured independently at various points. This wavelength shift was then applied directly to the ambient data to obtain the cryogenic spectra.

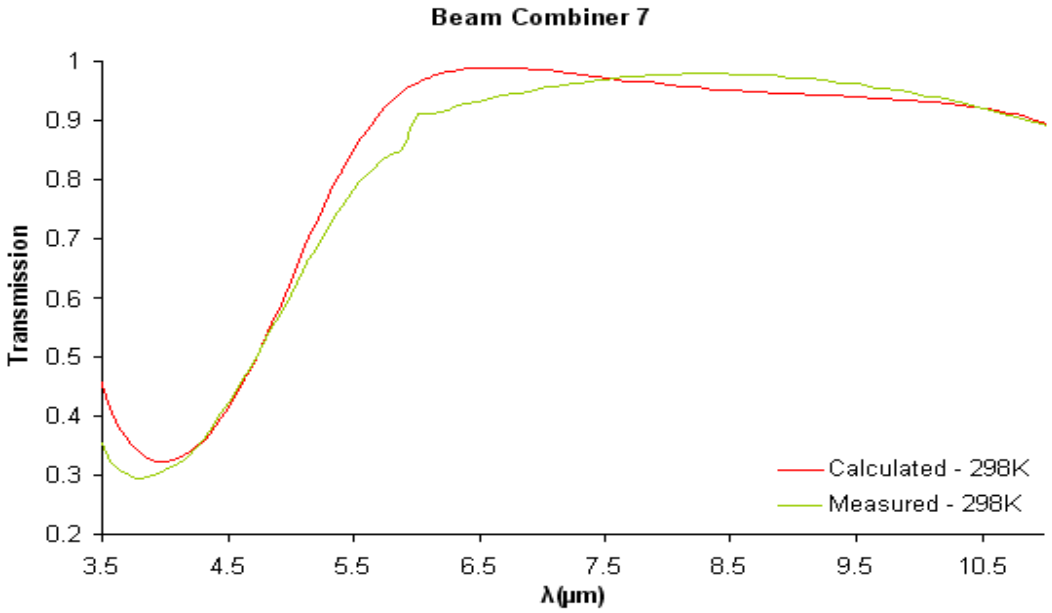


Figure 4.4: Beam combiner 7 at ambient temperature calculation (red) and measurement (green).

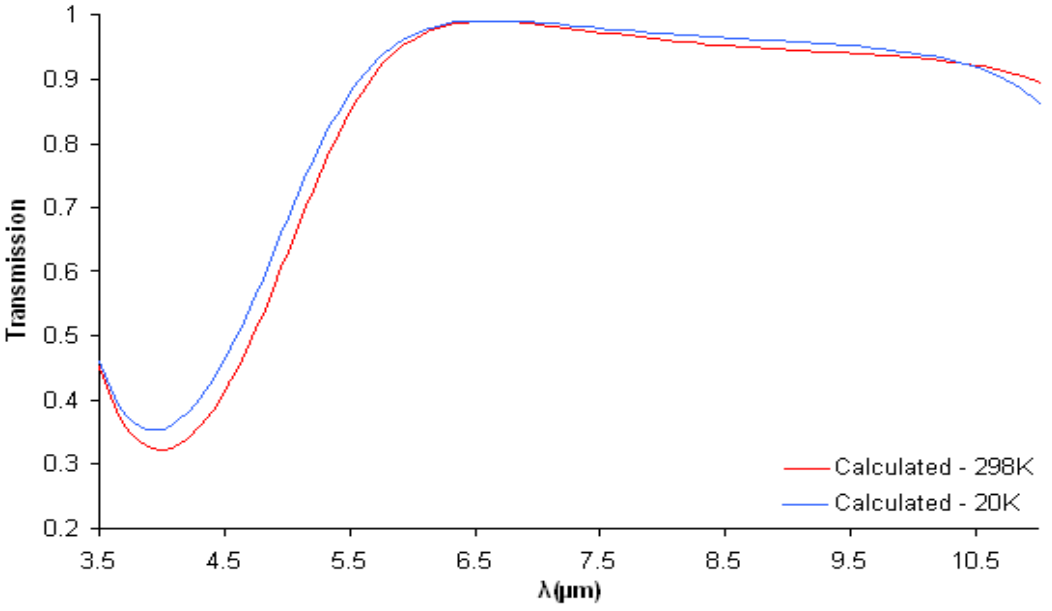


Figure 4.5: Calculation results for beam combiner 7 at 298K (red) and 20K (blue).

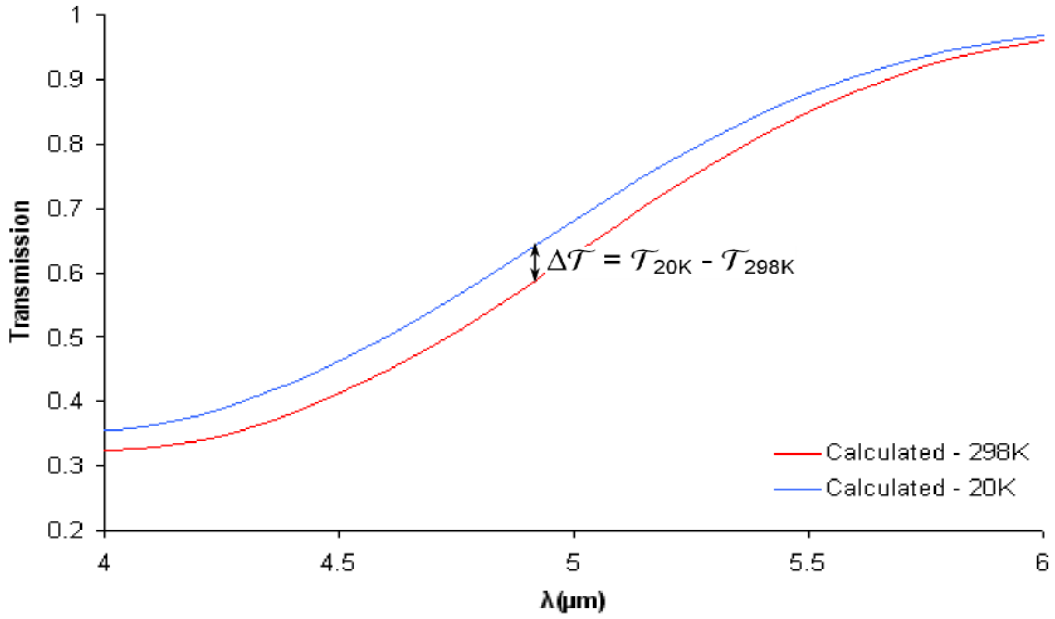


Figure 4.6: Example measurement of the transmission shift for BC7.

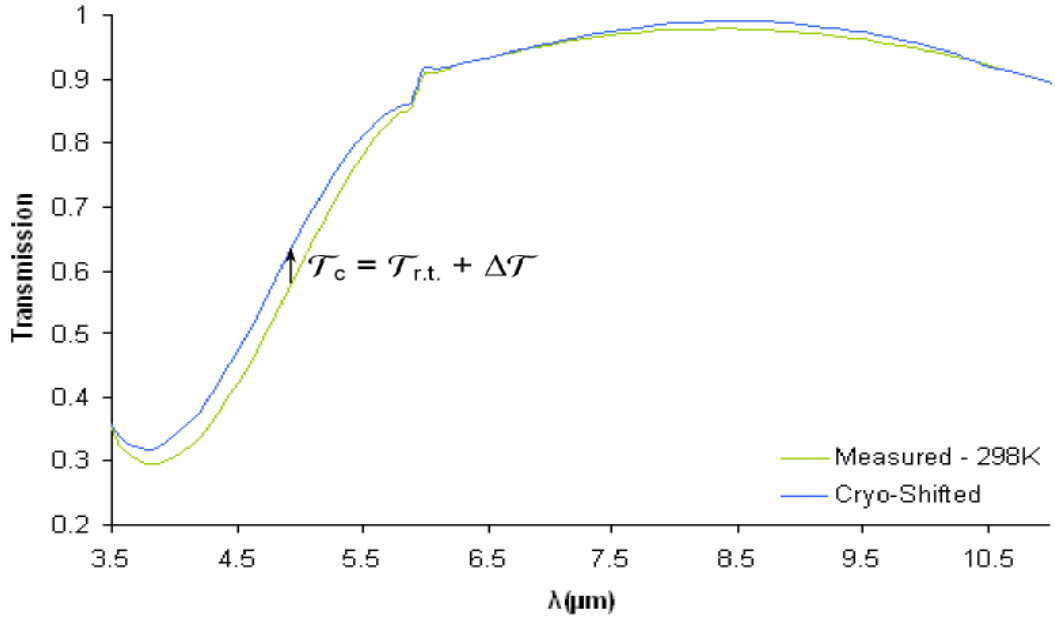


Figure 4.7: Beam combiner 7 shift application showing the room temperature and new cryogenic spectra.

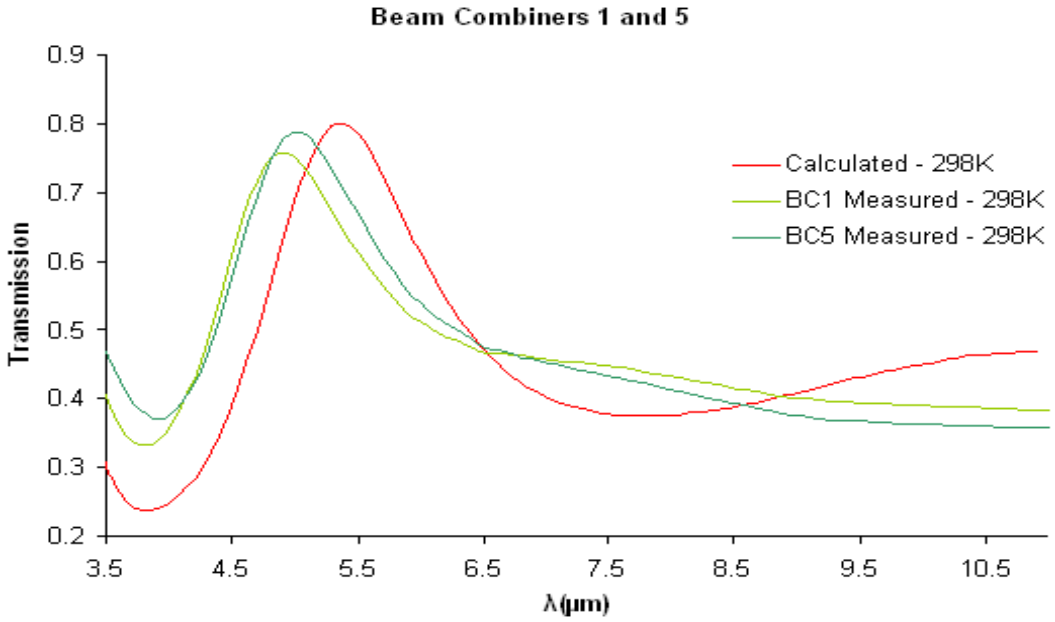


Figure 4.8: BC1 (light green) and BC5 (dark green) measurement shown with calculation at 298K (red).

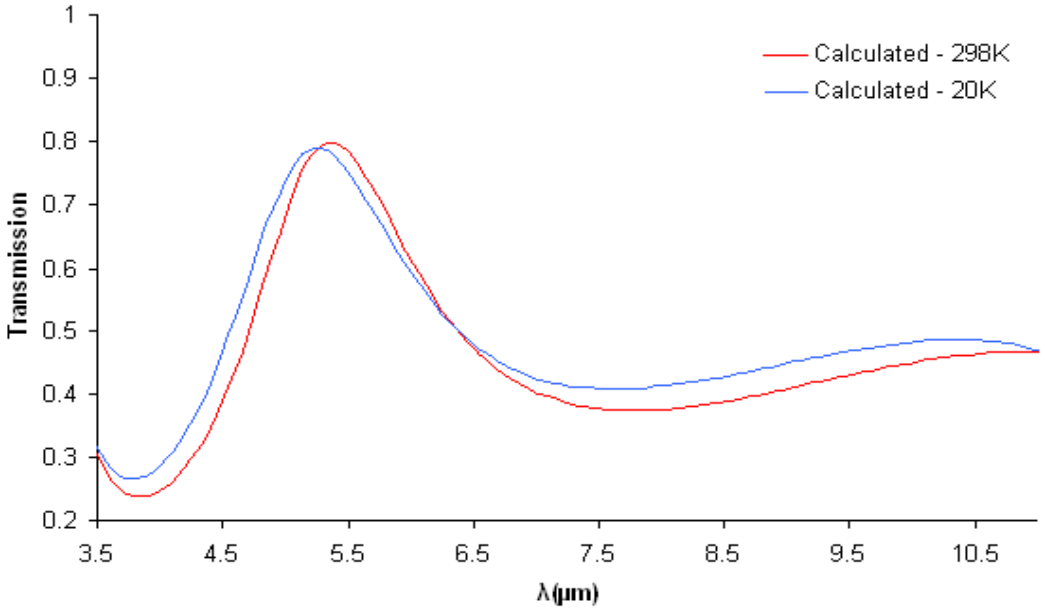


Figure 4.9: Calculation results for beam combiners 1 and 5 at 298K (red) and 20K (blue).

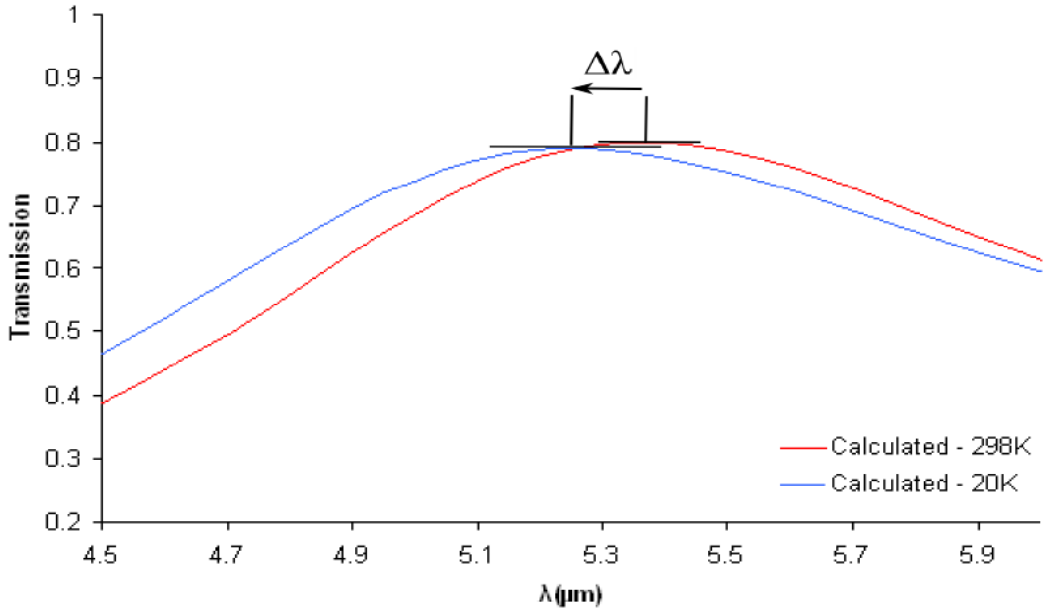


Figure 4.10: Example measurement of wavelength shift where the features of the calculation do not align with the measured features for BC1 and BC5.

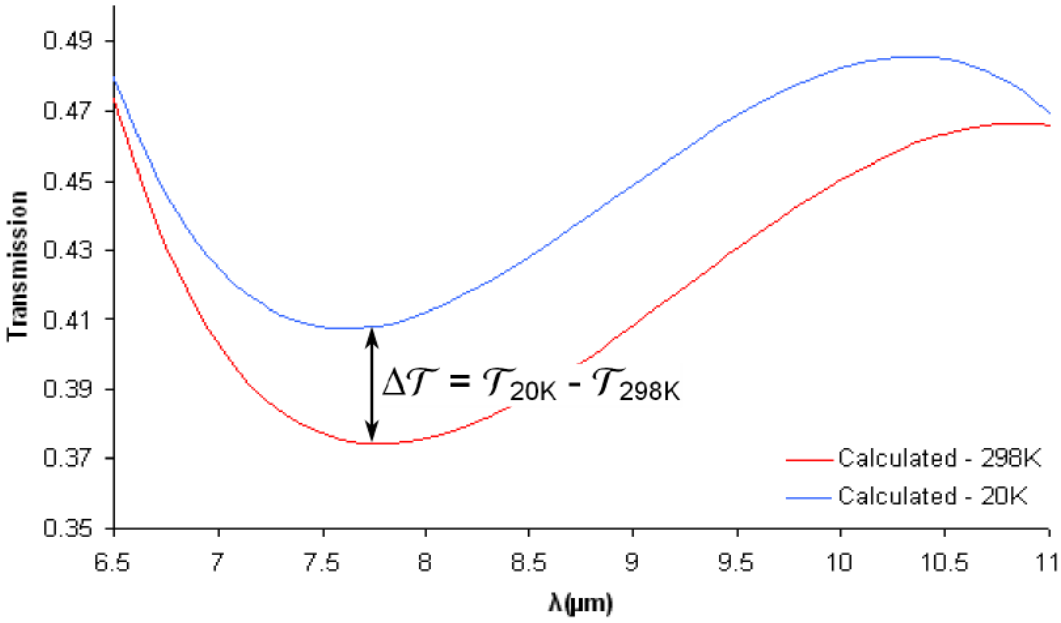


Figure 4.11: Example determination of transmission shift in the band of interest where agreement between calculation and measurement is better.

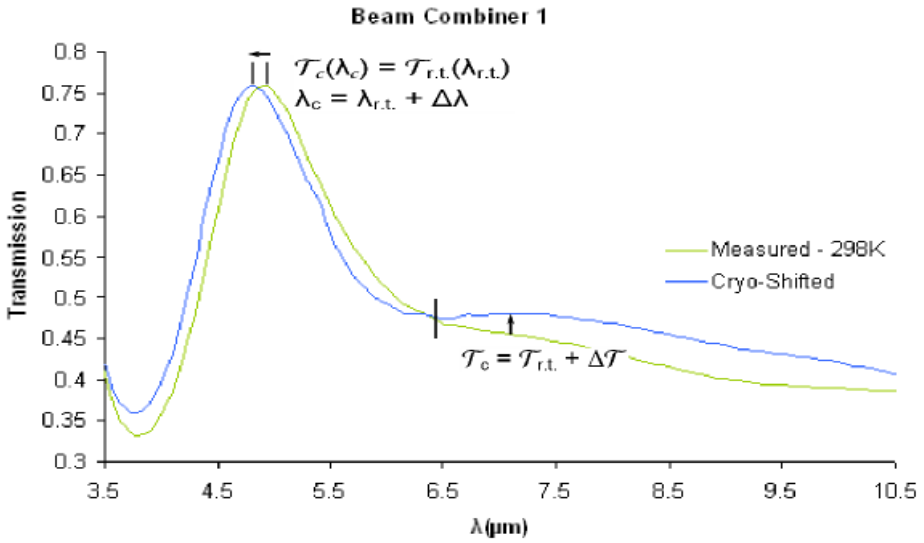


Figure 4.12: Beam combiner-1 spectral data before and after cryo-shift. To the left of the line, $\Delta\lambda$ was applied while the transmission was held constant. Right of the line, the shift was applied through direct addition of $\Delta\mathcal{T}$ while lambda was held constant.

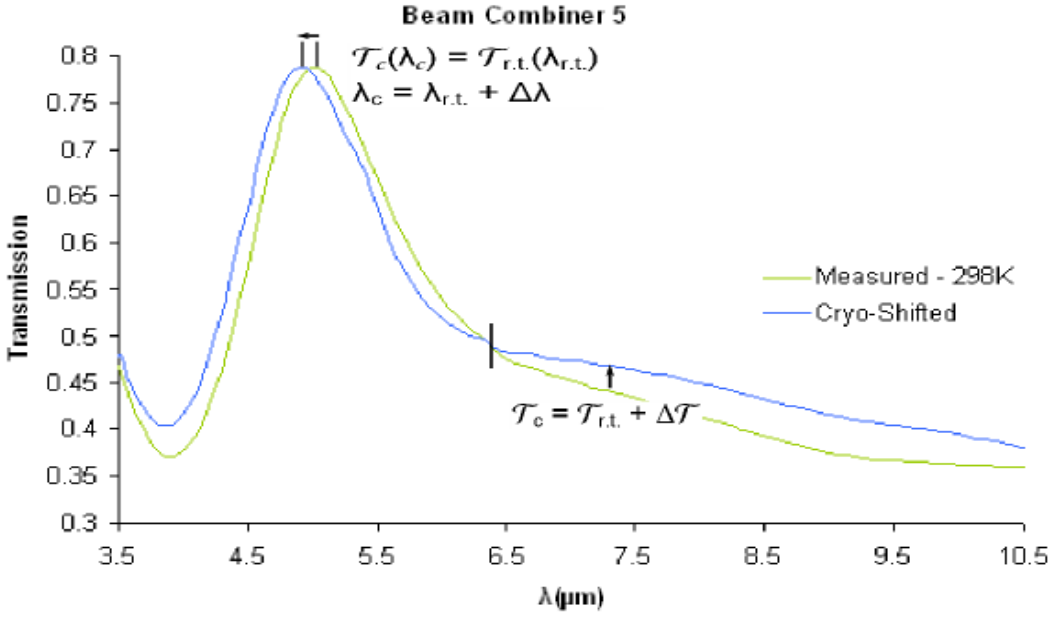


Figure 4.13: Beam combiner-5 spectral data before and after cryo-shift. To the left of the line, $\Delta\lambda$ was applied while the transmission was held constant. Right of the line, the shift was applied through direct addition of $\Delta\mathcal{T}$ while lambda was held constant.

4.2 Bandpass Filters Cryogenic Characterization

The coating prescriptions for the selected bandpass filters were deemed proprietary by the vendor. However, the vendor did supply witness measurements at cryogenic temperatures for the band 1 and band 2 filters and the materials used in the coatings. To supplement this data, a prescription for a wide bandpass filter (courtesy of Software Spectra, Inc. [SSI, 2007]) having a similar mid-infrared bandpass and using the same materials, zinc sulfide and germanium, as the components was input into the calculation program. The calculation results from the Software Spectra filter together with the cryogenic witness data was used to apply a shift to the ambient data of the three components, thus obtaining cryogenic spectra for use in the radiometric model (see figures 4.14 - 4.24). The application was performed by measuring the wavelength and transmission shift across the spectra of the witness measurements. A line was then fit to the measurements and used to calculate the shifts for the actual filters. Since there was no witness data or design prescriptions available for the band 1+2 filter, the average of the measured shifts of the witnesses was used. Arbitrary units are used for these graphs for the purpose of security.

The Software Spectra, Inc. wide bandpass filter used as a supplement consist of forty seven layers of alternating zinc sulphide and germanium all deposited on one side of a thick germanium substrate. The Software Spectra website states a design bandpass of three to five microns for this prescription [SSI, 2007]. While the actual prescriptions for the bandpass filters are not known, it is known that the coating materials are germanium and zinc sulphide and that they are deposited on a thick germanium substrate. Therefore, it was assumed that this would be a good substitute for the calculation program for determining cryogenic properties of these types of bandpass filters due to the similarities in bandpass, materials, and substrate. Shown in figure 4.25 is a comparison of the calculation program's results and the results from a publicly available optics analysis program called FreeSnell. FreeSnell uses constant refractive index values, as given in the prescription, of 2.2 for zinc sulphide, 4.2 for germanium layer, and 4 for germanium substrate [Jaffer, 2006]. For the comparison, the calculation program was changed to use those same constant values. The same calculation was re-run, figure 4.26, using the temperature dependent dispersion relations from chapter 2 to find the temperature dependence of the filter. As figure 4.26 shows, the shift calculated by the program is in pretty good agreement with the measured shifts of the band 1 and band 2 filter witnesses in that the wavelength shift is largest at the cut-on point and decreases slightly over the bandpass until the cut-off point. This served to show that the calculation program was performing as expected.

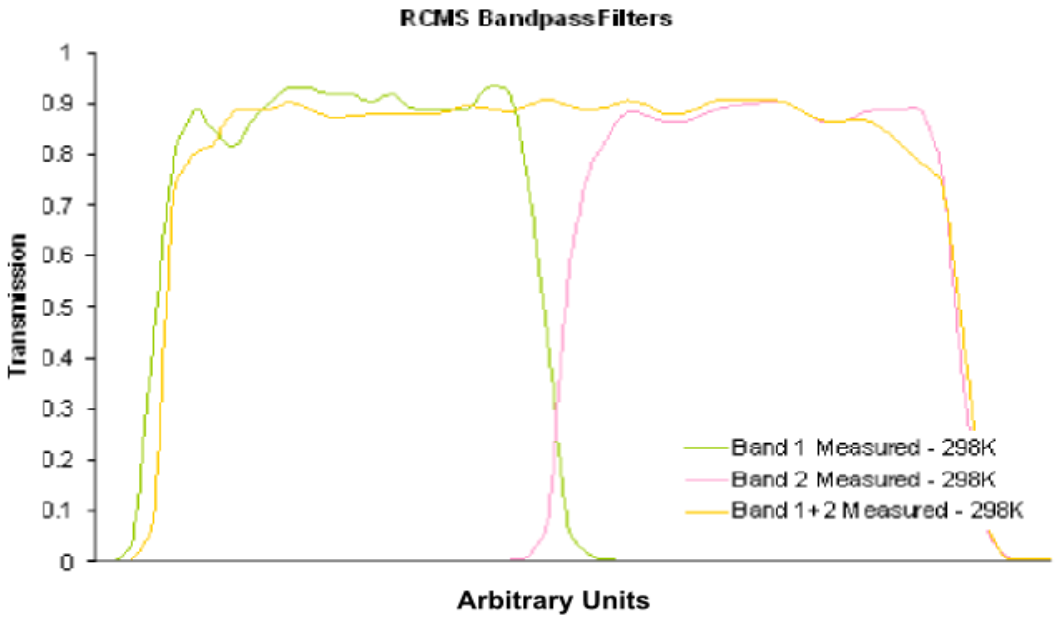


Figure 4.14: The measured spectra of the three selected bandpass filters.

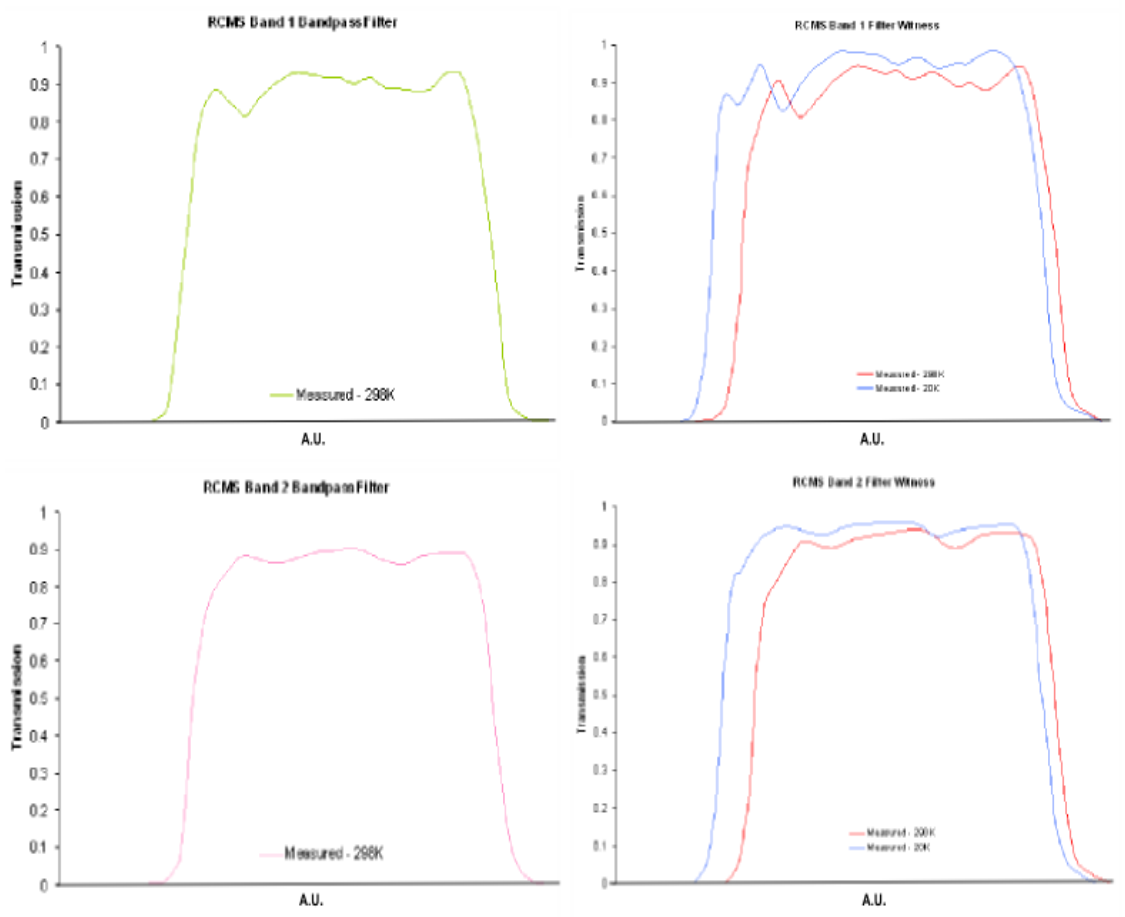


Figure 4.15: The band 1 and band 2 bandpass filters ambient measurements shown with their respective witness measurements at room temperature and 20K.

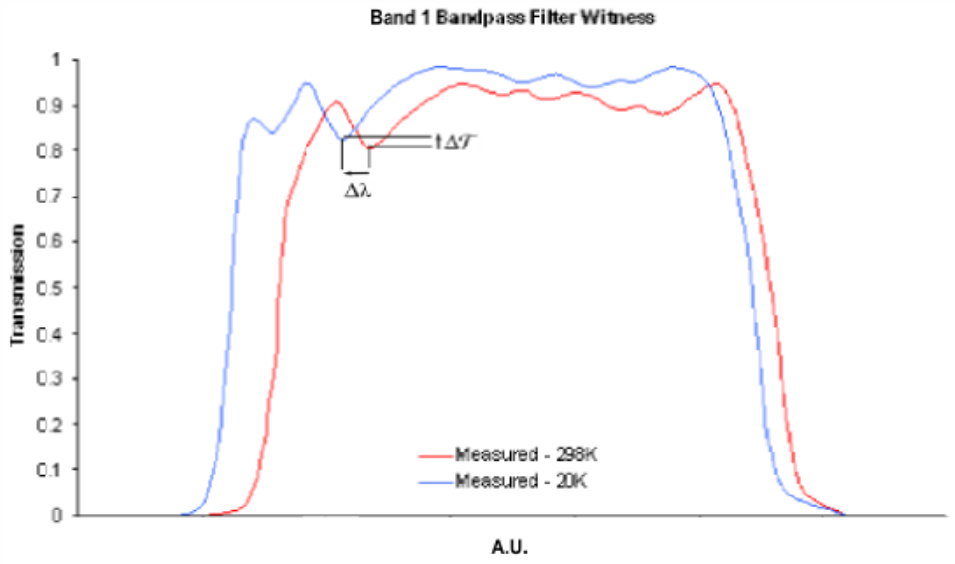


Figure 4.16: Example of a wavelength and transmission shift measurement for the band 1 filter witness.

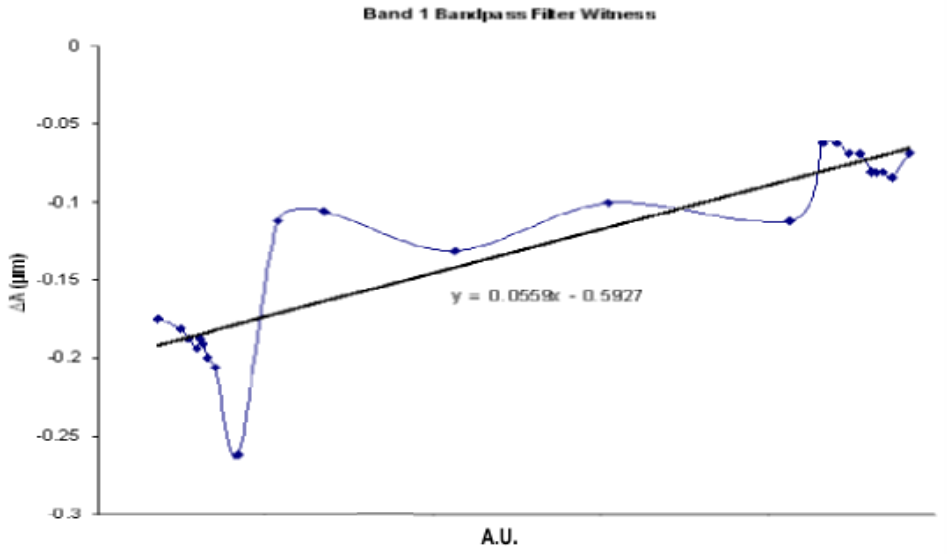


Figure 4.17: The wavelength shift for the band 1 filter as a function of the ambient wavelength.

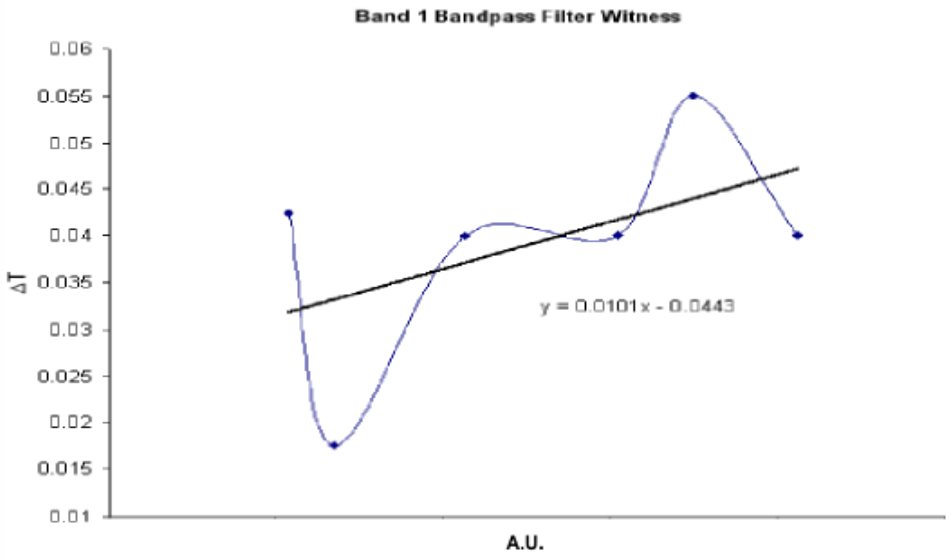


Figure 4.18: The transmission shift for the band 1 filter as a function of the ambient wavelength.

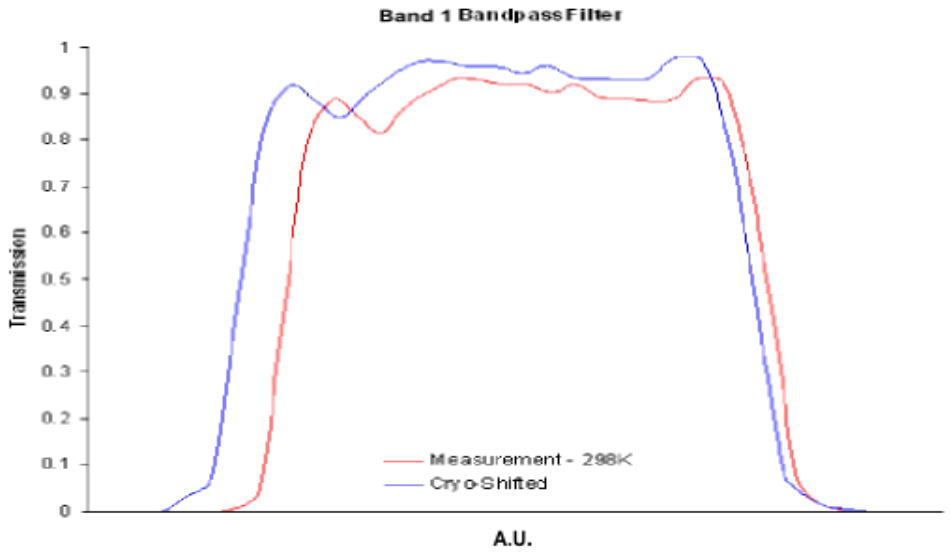


Figure 4.19: The ambient measurement and the new cryogenic spectrum after applying the measured shifts from the witness.

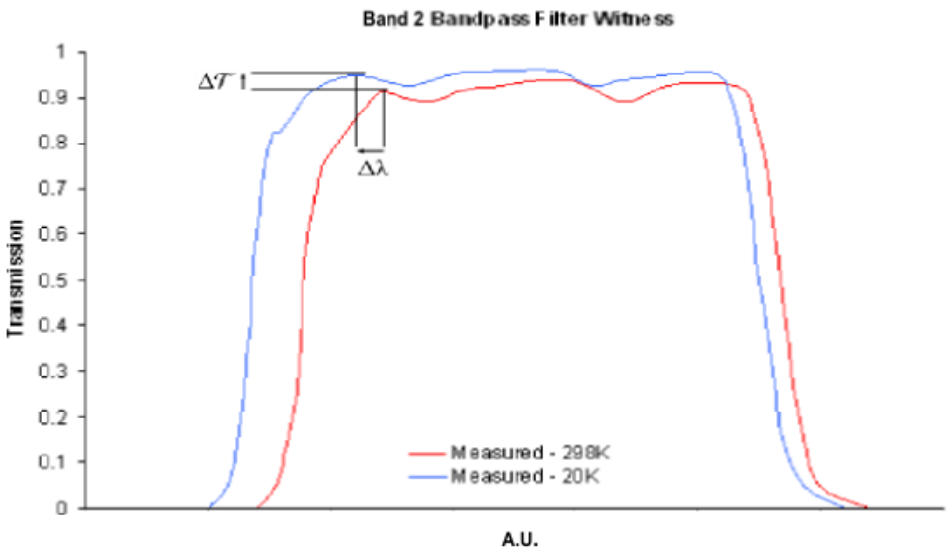


Figure 4.20: Example of a wavelength and transmission shift measurement for the band 2 filter witness.

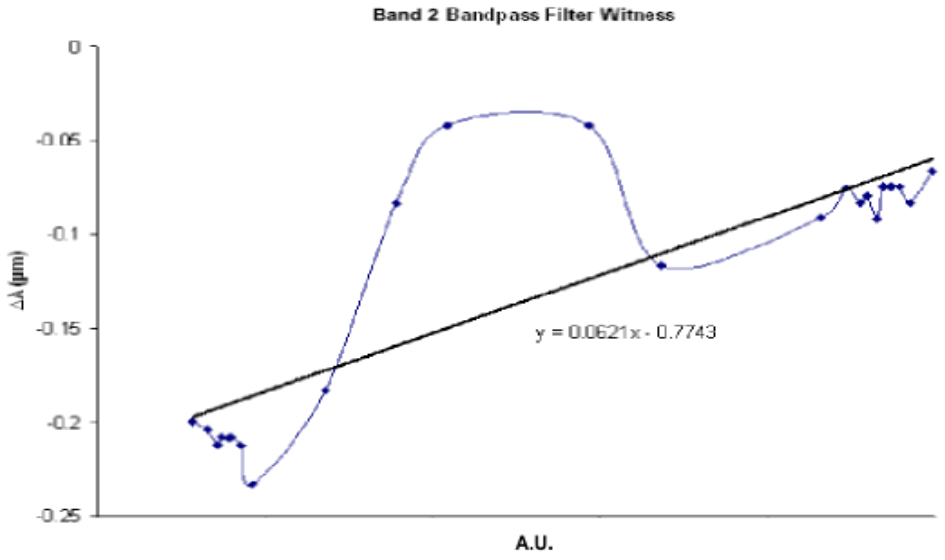


Figure 4.21: The wavelength shift for the band 2 filter as a function of the ambient wavelength.

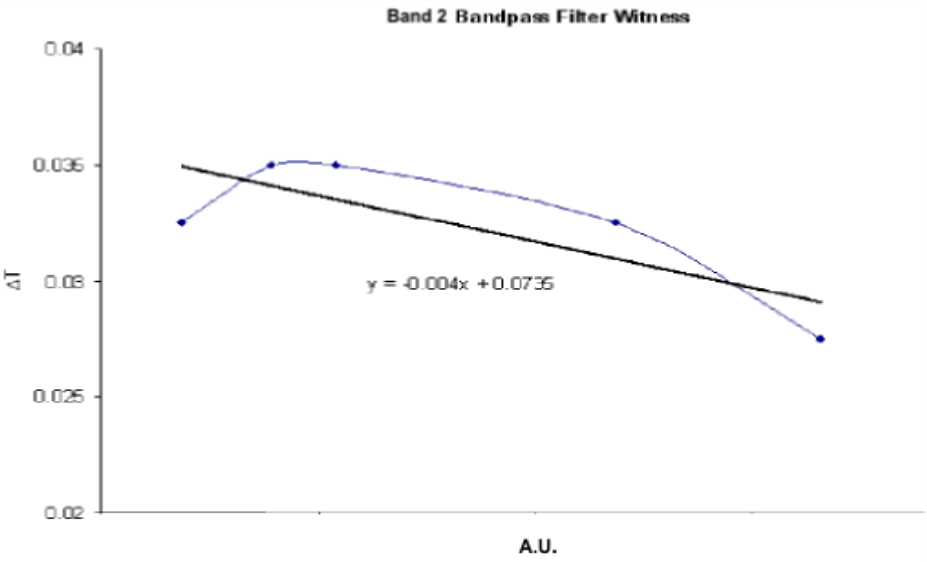


Figure 4.22: The transmission shift for the band 2 filter as a function of the ambient wavelength.

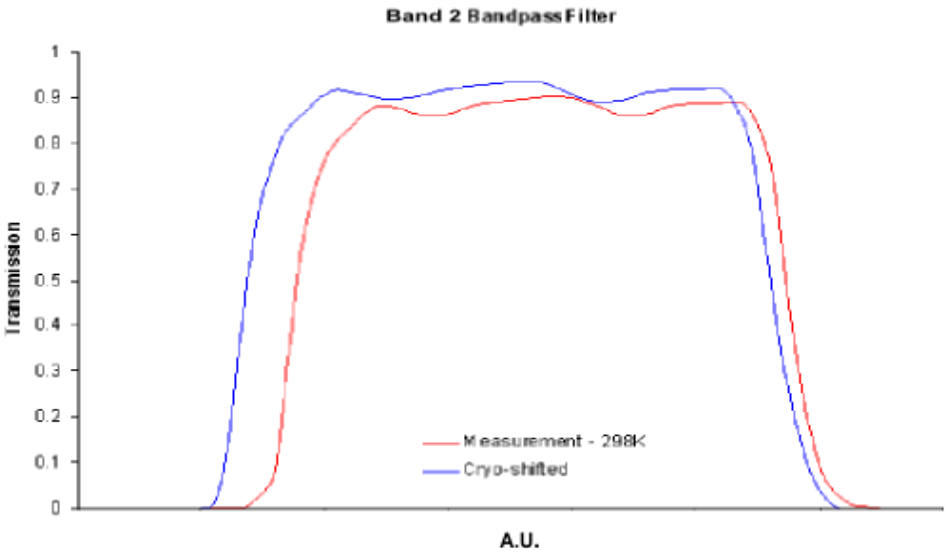


Figure 4.23: The ambient measurement and the new cryogenic spectrum after applying the measured shifts from the witness.

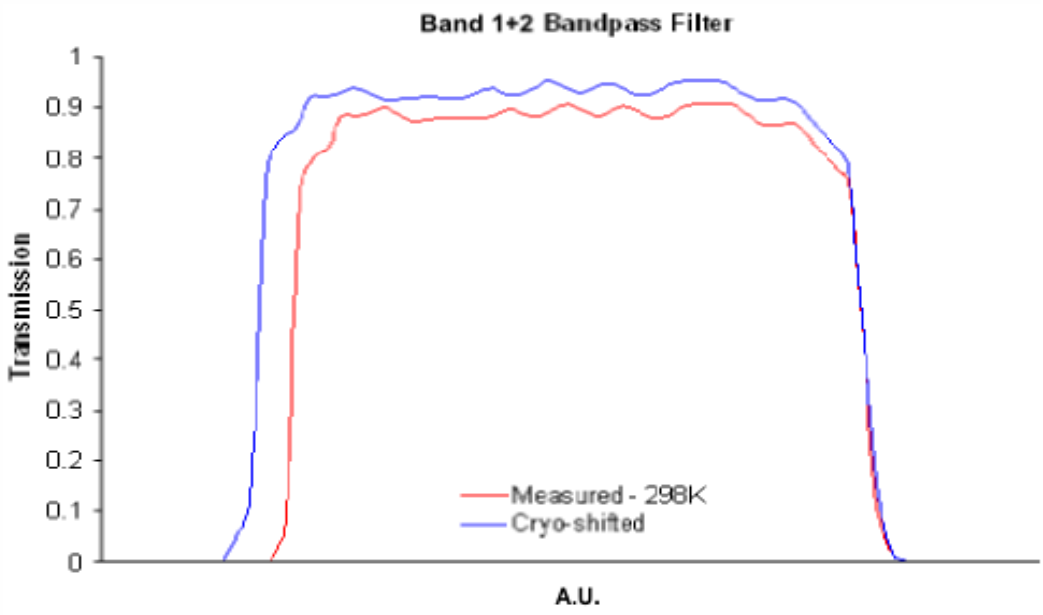


Figure 4.24: The ambient measurement and the new cryogenic spectrum after applying the averaged shifts.

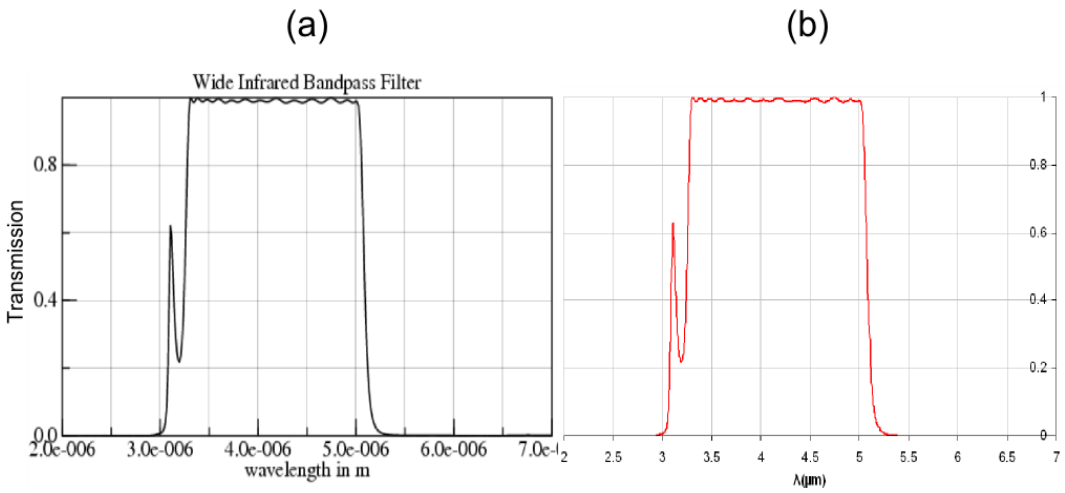


Figure 4.25: The calculation results for the Software Spectra, Inc. wide bandpass filter prescription using constant refractive indices (a) from FreeSnell, and (b) from the calculation program.

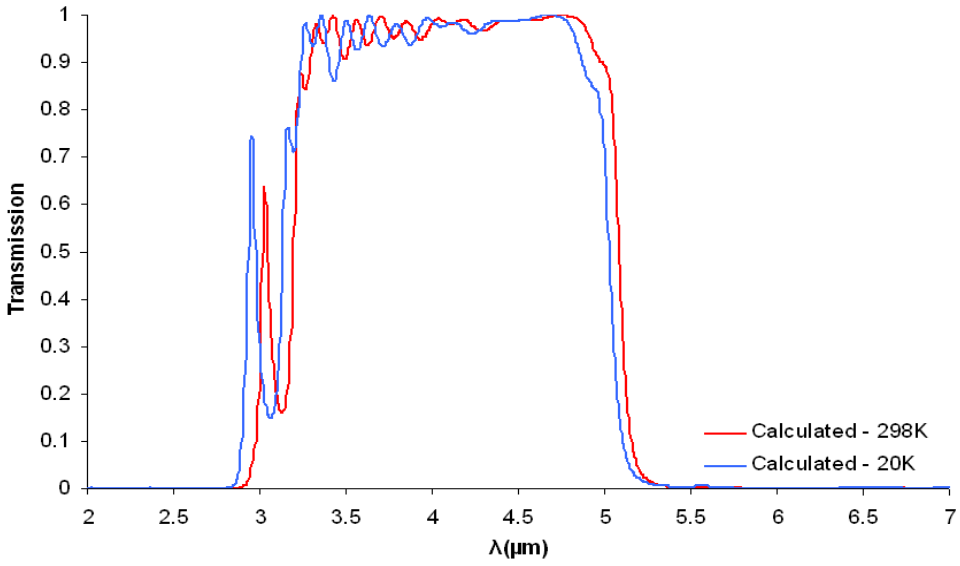


Figure 4.26: The calculation results for the Software Spectra, Inc. wide bandpass filter prescription using the temperature dependent dispersion relations from section 1.2 for germanium and zinc sulphide.

Chapter 5

The Chamber Model and Results

The computer model of the cryo-vacuum chamber uses the spectral profiles of all the components in the chamber to determine an expected throughput for a given situation. It is based upon the basic optical principle that output of an optical system is the input times the transmission, (or reflection if that path is desired), of the optics. Beginning with the irradiance of the source(s), each component characteristic along the radiation path is multiplied by the previous until finally yielding the irradiance at the aperture of the sensor. Polarization of the radiation by reflection off of elements with a large angle of incidence is accounted for by allowing each polarization to propagate through independently before averaging. As part of a chamber checkout, the blackbody sources were isolated and measured with the RCMS gallium-doped silicon detector at source temperatures of 400K and 700K. This path sent the radiation through all three beam combiners and all three bandpass filters, (individually), before being measured (see figure 5.1).

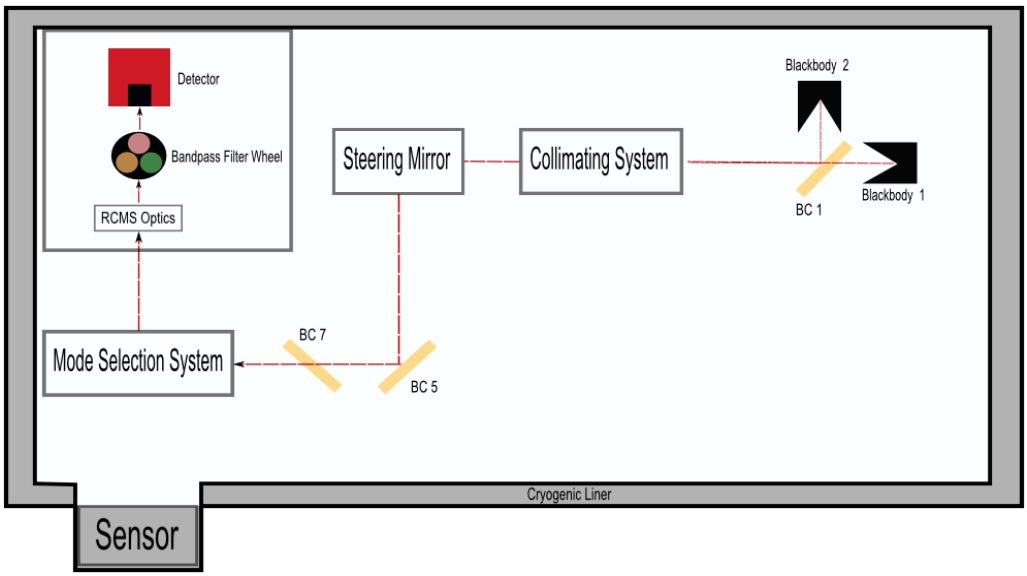


Figure 5.1: Diagram of the measured radiation paths.

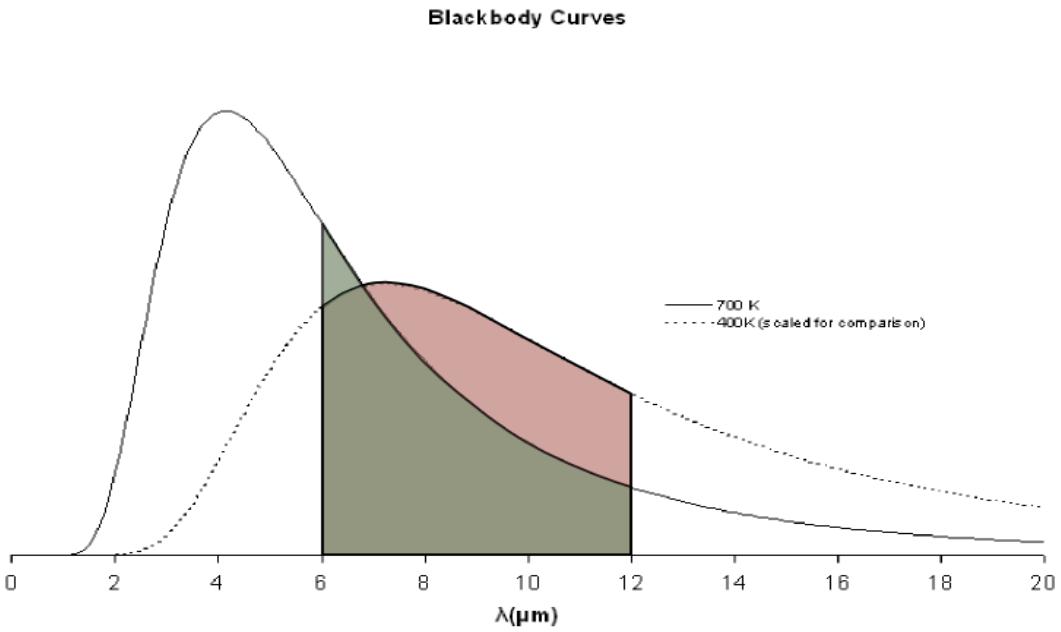


Figure 5.2: Blackbody curves highlighting the 6-l2 μm range.

The gallium-doped silicon detector has an effective response range of 1-25μm. As such, the model integrates the expected throughput over the 1-25μm range for comparison with the measurements. The measurements are expressed as a series of points with each point corresponding to different wavelength ranges as different filters are used in front of the detector emphasizing the mid-infrared region (see figure 5.2). The points 3, 4, and 5 shown below correspond to the band 1, 2, and 1+2 bandpass filters, respectively (see figures 5.3 - 5.6).

As the figures show, the model performance is quite different, more than anticipated actually, after accounting for cryogenic temperature in the spectra of the selected components (see figure 5.7). The model seems to predict point 3 as consistently higher relative to the measurement than points 4 or 5. This did not change after applying the cryo-shifts and, as a result, the cryo-shifted model prediction for point 3 is consistently high. Point 4 shows better agreement after applying the cryo-shifts and is nearly perfect in most cases. Point 5, like 3, is also consistently high relative to the measurements. One hypothesis to explain this, in conjunction with point 3, is that another component in the path is affecting band 1. It should be mentioned that some common infrared materials, lead telluride for example, do have positive $\frac{\Delta\lambda}{\Delta T}$'s which would result in their spectra shifting to longer wavelengths thereby canceling some of the shifts applied here [Feng and Yan, 1992].

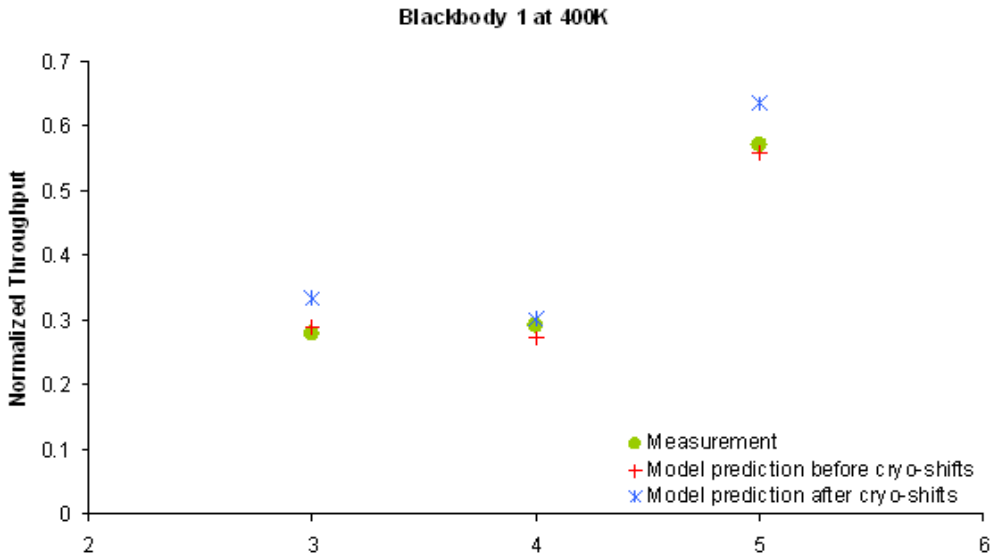


Figure 5.3: The throughput of blackbody 1 at 400K before (red) and after (blue) cryo-shifting of the selected components shown with measurement.

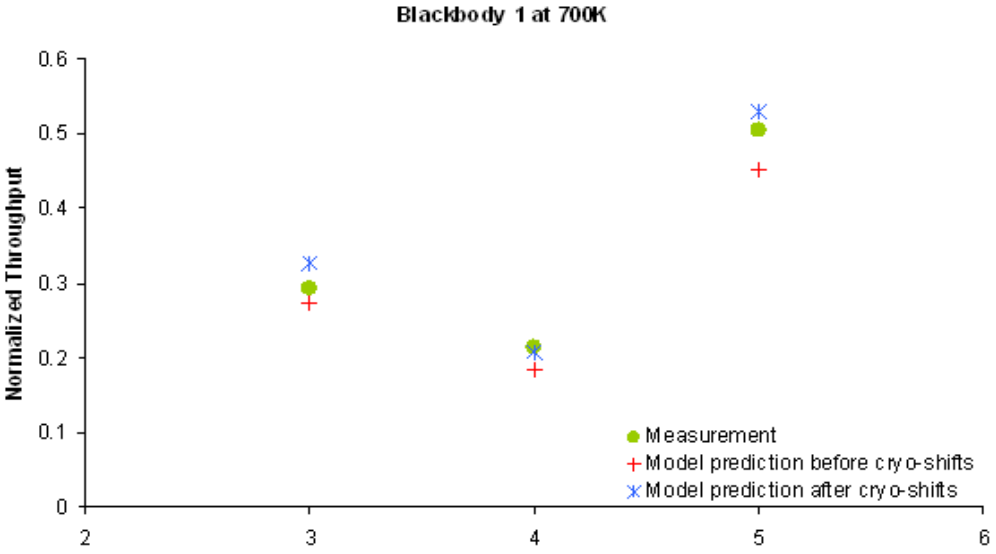


Figure 5.4: The throughput of blackbody 1 at 700K, model and measurement results. Point 3 is the band 1 filter. Point 4 is the band 2 filter. Point 5 is the band 1+2 filter.

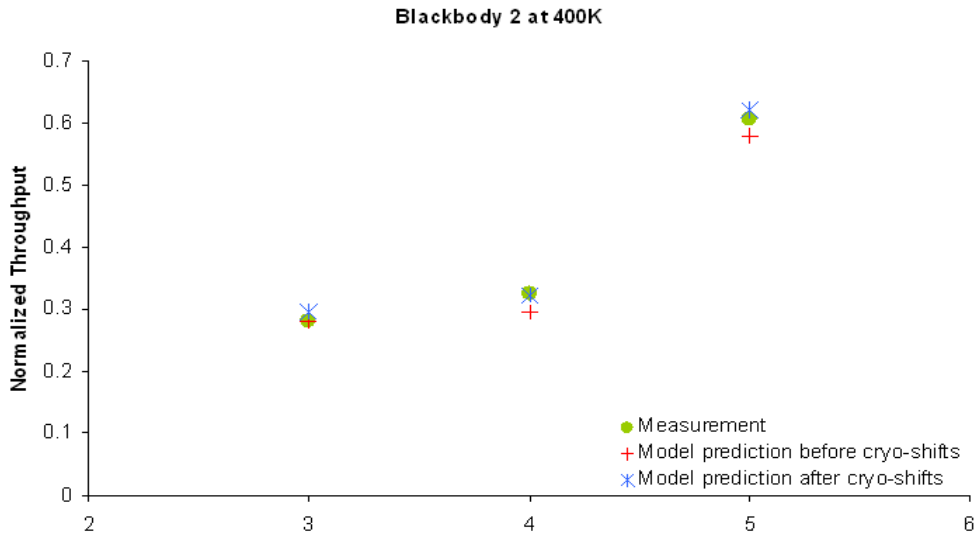


Figure 5.5: The throughput of blackbody 2 at 400K before (red) and after (blue) cryo-shifting of the selected components shown with measurement.

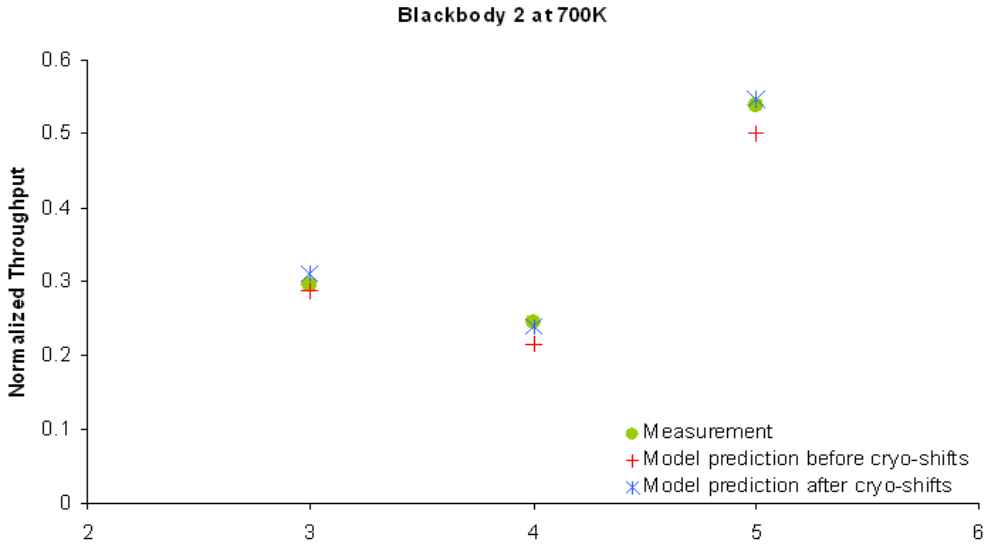


Figure 5.6: The throughput of blackbody 2 at 700K, model and measurement results. Point 3 is the band 1 filter. Point 4 is the band 2 filter. Point 5 is the band 1+2 filter.

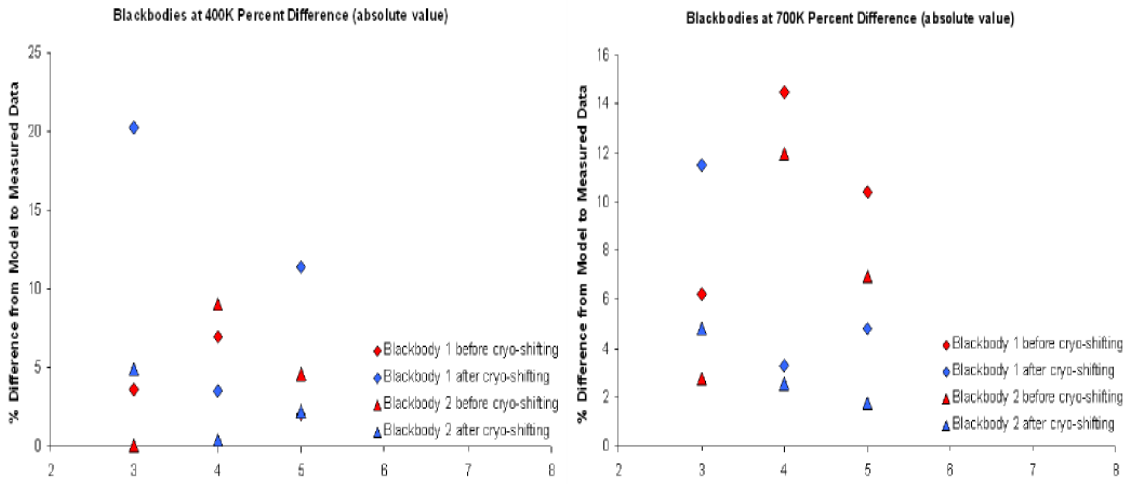


Figure 5.7: A before and after comparison of the 10V model. The left chart shows the absolute value percent difference between test data and model prediction with the blackbodies at 400K. The right chart shows the same with blackbodies at 700K.

Chapter 6

Conclusion

The temperature dependence of selected multilayer optical components, including double sided beam combiners and single sided bandpass filters, has been analyzed by using temperature dependent dispersion relations in the characteristic matrix method. The results of the calculations, along with measurements, were applied to the measured room temperature spectra of the components to give a characterization of the components at cryogenic temperatures. The new cryogenic spectra were then used in the computer model of the 10V chamber to give a more accurate prediction of the chambers output which is essential to proper calibration of the chamber.

6.1 Future Research

The components selected for this work are just a few of many in the cryo-vacuum chamber chosen for this investigation. The model of the chamber would certainly benefit from cryogenic characterization of other components. The calculation program could be enhanced by dispersion relations that hold outside of the primary transmission region of the materials, specifically over the full range of the detector. For this feat to be accomplished, the extinction coefficient of the layers and substrate would undoubtedly also have to be included in the program so that the absorption bands in the materials would be accurately predicted. The program could also be upgraded to be able to predict the performance of metal components, such as gold plated mirrors, as opposed to only dielectrics. Also, this work could be extended to include components from other cryo-vacuum chambers which are of similar design and purpose. Any of this work would be beneficial to the integrity of the model and to calibration of the chamber which, in turn, would help ensure the proper testing and characterization of the sensor systems that the chamber was designed for.

Bibliography

Bibliography

[Arfken and Weber, 2001] Arfken, G. B. and Weber, H. B. (2001). *Mathematical Methods for Physicist*, pages 472 – 473. Academic Press, San Diego, California, 5th edition.

[Barnes and Piltch, 1979] Barnes, N. and Piltch, M. (1979). Temperature dependent sellmeier coefficients and non-linear optics average power limit for germanium. *J. Opt. Soc. Am.*, 69:178.

[Born and Wolf, 1964] Born, M. and Wolf, E. (1964). *The Principles of Optics*, pages 51 – 60. Pergamon Press, Oxford, 2nd edition.

[Feldman et al., 1978] Feldman, A., Horowitz, D., Waxler, R., and Dodge, M. (1978). Optical materials characterization - final technical report. Technical Report 933, National Bureau of Standards, Center for Materials Science, National Measurements Laboratory, Washington D.C.

[Feng and Yan, 1992] Feng, W. and Yan, Y. (1992). Shift in infrared interference filters at cryogenic temperature. *Applied Optics*, 31:6591–6592.

[Hawkins, 1998] Hawkins, G. H. (1998). *Spectral characterisation of infrared optical materials and filters [Electronic Version]*. PhD thesis, The University of Reading, Infrared Laboratory.

[Icenogle et al., 1976] Icenogle, H., Platt, B. C., and Wolfe, W. L. (1976). Refractive indices and temperature coefficients of germanium and silicon [electronic version]. *Applied Optics*, 15:2348.

[IML, 2007] IML (2007). Infrared multilayer laboratory. Instrumentation and Signal Processing Research Group, School of Systems Engineering, The University of Reading, UK, Retrieved June 2007, Web Site: http://www.irfilters.reading.ac.uk/.

[Jaffer, 2006] Jaffer, A. (2006). FreeSnell. Retrieved January 15, 2007, Web Site: http://swiss.csail.mit.edu/ jaffer/FreeSnell/.

[Kodak, 1967] Kodak (1967). Irtran infrared optical material condensed data sheet. Technical Report U-71, Eastman Kodak Co., Rochester, NY.

[Lowry et al., 2004a] Lowry, H., Crider, D., Goethert, W., and Bertrand, W. (2004a). Implementation of scene simulation technologies in the AEDC space chambers. In *Proceedings of SPIE*, volume 5408, pages 84–95.

[Lowry et al., 2004b] Lowry, H., Nicholson, R., Simpson, R., Mead, K., and Crider, D. (2004b). Ground testing of space-based imaging sensors in AEDC's space chambers. In *24th AIAA Aerodynamic Measurement Technology and Ground Testing Conference*, Portland, OR. Paper number 2194.

[Marple, 1964] Marple, D. (1964). Refractive index of ZnSe, ZnTe, and CdTe. *J. Appl. Phys.*, 35:539–542.

[Moses, 1970] Moses, A. (1970). Refractive index of optical materials in the infrared region [electronic version]. Technical Report DS-166, Electronic Properties Information Center, Hughes Aircraft Company, Culver City, California.

[Norton, 1962] Norton (1962). Properties and literature references on magnorite fused magnesium oxide. Technical Report P-1.5-1, Norton Co. Refractories Division, Worcester, MA.

[Palik, 1991] Palik, E. D. (1991). *Handbook of Optical Constants of Solids II*, page 1054. Academic Press, London.

[Poelman and Smet, 2003] Poelman, D. and Smet, P. (2003). Methods for the determination of the optical constants of thin films from single transmission measurements: a critical review [electronic version]. *J. Phys D: Appl. Phys.*, 36:1850 – 1857.

[Robb and Mercado, 1983] Robb, P. N. and Mercado, R. (1983). Calculation of refractive indices using Buchdahl's chromatic coordinate [electronic version]. *Applied Optics*, 22:1198–1215.

[Salzberg and Villa, 1958] Salzberg and Villa (1958). Index of refraction of germanium. *Optical Society of America*, 48:579.

[SSI, 2007] SSI (2007). Software Spectra thin film coating examples. Software Spectra, Inc., Retrieved January 20, 2007, Web Site: http://www.sspectra.com/examples.html.

[Stephens and Malitson, 1952] Stephens, R. and Malitson, I. (1952). Index of refraction of magnesium oxide [electronic version]. *Journal of Research of Natl. Bur. Stand.*, 49:249–252.

[Sullivan and Dobrowolski, 1992] Sullivan, B. and Dobrowolski, J. (1992). Deposition error compensation for multilayer coatings. *Applied Optics*, 31:3821 – 3835.

Appendix

Appendix A

Derivation of the Characteristic Matrix of a Homogeneous Dielectric Thin Film

Specifying to a homogeneous dielectric material means that ϵ, μ, and $n = \sqrt{\epsilon\mu}$ are all constants with respect to z [Born and Wolf, 1964]. Equations 3.15 and 3.16 become

$$\frac{\partial^2 V(z)}{\partial z^2} + (k_0^2 n^2 \cos^2\theta)V(z) = 0, \tag{A.1}$$

$$\frac{\partial^2 Z(z)}{\partial z^2} + (k_0^2 n^2 \cos^2\theta)Z(z) = 0. \tag{A.2}$$

They are subject to the constraints 3.12 and 3.14:

$$\frac{\partial V(z)}{\partial z} = ik_0(\epsilon - \frac{\alpha^2}{\mu})Z(z),$$

$$\frac{\partial Z(z)}{\partial z} = ik_0\mu V(z).$$

The solutions are

$$V = \frac{1}{i}\sqrt{\frac{\epsilon}{\mu}}\cos\theta(B\cos(k_0 nz\cos\theta) - A\sin(k_0 nz\cos\theta)), \tag{A.3}$$

$$Z = A\cos(k_0 nzcos\theta) + B\sin(k_0 nz\cos\theta). \tag{A.4}$$

Therefore, the particular solutions,

$$Z_1' = ik_0\mu V_1, \qquad Z_2' = ik_0\mu V_2, \text{ and}$$

$$V_1' = ik_0(\epsilon - \tfrac{\alpha^2}{\mu})Z_1, \quad V_2' = ik_0(\epsilon - \tfrac{\alpha^2}{\mu})Z_2,$$

become

$$Z_1 = \frac{i}{\cos\theta}\sqrt{\frac{\mu}{\epsilon}}\sin(k_0 nz\cos\theta), \tag{A.5}$$

$$V_1 = \cos(k_0 nz\cos\theta), \tag{A.6}$$

$$Z_2 = \cos(k_0 nz\cos\theta), \tag{A.7}$$

$$V_2 = i\cos\theta\sqrt{\frac{\epsilon}{\mu}}\sin(k_0 nz\cos\theta), \tag{A.8}$$

where α has been replaced by $\alpha = n\sin\theta$. Since $Z_1 = f(z)$, $Z_2 = F(z)$, $V_1 = g(z)$, $V_2 = G(z)$, and from 3.27 we have

$$\mathcal{M} = \begin{pmatrix} g(z) & -f(z) \\ -G(z) & F(z) \end{pmatrix},$$

the characteristic matrix is seen to become

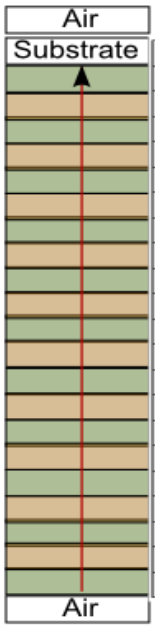
$$\mathcal{M} = \begin{pmatrix} \cos(k_0 nz\cos\theta) & -\frac{i}{p}\sin(k_0 nz\cos\theta) \\ -ip\sin(k_0 nz\cos\theta) & \cos(k_0 nz\cos\theta) \end{pmatrix}, \tag{A.9}$$

where the definition of p, ($p = \sqrt{\frac{\epsilon}{\mu}}\cos\theta$), has been used.

Appendix B

Example Multilayer Calculation

As an example, consider the following 21 layer mirror prescription, (see figure B.1), under radiation of wavelength λ and at normal incidence.



Layer	Index	Thickness (microns)
0	H	.04421
1	L	.10257
2	H	.04397
3	L	.07313
4	H	.04256
5	L	.08252
6	H	.04892
7	L	.08718
8	H	.04648
9	L	.06656
10	H	.03616
11	L	.16254
12	H	.05307
13	L	.09719
14	H	.07913
15	L	.10219
16	H	.06777
17	L	.12887
18	H	.05324
19	L	.15861
20	H	.03440

Figure B.1: Prescription for a cold mirror designed to reflect shorter wavelengths and transmit longer ones, courtesy of Software Spectra, Inc [SSI, 2007].

For simplicity, assume the refractive indices of the materials to be constant with $n_H = 2.4$, $n_L = 1.46$, and $n_{Sub} = 1.52$ with the materials being all dielectric such that $\mu \approx 1$, $p \approx \sqrt{\epsilon} = n$, and $q \approx \sqrt{\frac{1}{\epsilon}} = \frac{1}{n}$. From A.9, the characteristic matrix of layer 0 for a TE wave is seen to be

$$\mathcal{M}_0(\lambda) = \begin{pmatrix} \cos(\frac{2\pi}{\lambda} \times 2.4 \times .04421) & -\frac{i}{2.4}\sin(\frac{2\pi}{\lambda} \times 2.4 \times .04421) \\ -i\,2.4\sin(\frac{2\pi}{\lambda} \times 2.4 \times .04421) & \cos(\frac{2\pi}{\lambda} \times 2.4 \times .04421) \end{pmatrix}.$$

The rest of the layers characteristic matrices would be found similarly. To find the total characteristic matrix of the stack, multiply all the matrices beginning with $\mathcal{M}_{20}$.

$$\mathcal{M}_{Tot} = \mathcal{M}_{20} \cdot \mathcal{M}_{19} \cdot \mathcal{M}_{18} \cdot \quad \ldots$$

E.g. for a wavelength of 500nm, $(.5\mu m)$, the characteristic matrix describing the multilayer would be

$$\mathcal{M}_{Tot}(.5) = \begin{pmatrix} \cos(\frac{2\pi}{.5} \times 2.4 \times .03440) & -\frac{i}{2.4}\sin(\frac{2\pi}{.5} \times 2.4 \times .03440) \\ -i\,2.4\sin(\frac{2\pi}{.5} \times 2.4 \times .03440) & \cos(\frac{2\pi}{.5} \times 2.4 \times .03440) \end{pmatrix}$$

$$\cdot \begin{pmatrix} \cos(\frac{2\pi}{.5} \times 1.46 \times .15861) & -\frac{i}{1.46}\sin(\frac{2\pi}{.5} \times 1.46 \times .15861) \\ -i\,1.46\sin(\frac{2\pi}{.5} \times 1.46 \times .15861) & \cos(\frac{2\pi}{.5} \times 1.46 \times .15861) \end{pmatrix}$$

$$\cdot \begin{pmatrix} \cos(\frac{2\pi}{.5} \times 2.4 \times .05324) & -\frac{i}{2.4}\sin(\frac{2\pi}{.5} \times 2.4 \times .05324) \\ -i\,2.4\sin(\frac{2\pi}{.5} \times 2.4 \times .05324) & \cos(\frac{2\pi}{.5} \times 2.4 \times .05324) \end{pmatrix}$$

$$\cdot \quad \ldots$$

$$\mathcal{M}_{Tot}(.5) = \begin{pmatrix} 2.98 & i\,.376 \\ i\,18.7 & -2.03 \end{pmatrix}$$

Which, by 3.35 and 3.36, gives transmission and reflection of

$$\mathcal{R} = .984,$$
$$\mathcal{T} = .016.$$

In this case, (normal incidence), calculation for a TM wave is not necessary as it will yield the exact same results.

B.1 Calculation Program Results

This prescription was input into the calculation program. For comparison, the results of the same prescription run in FreeSnell are also shown in figure B.2.

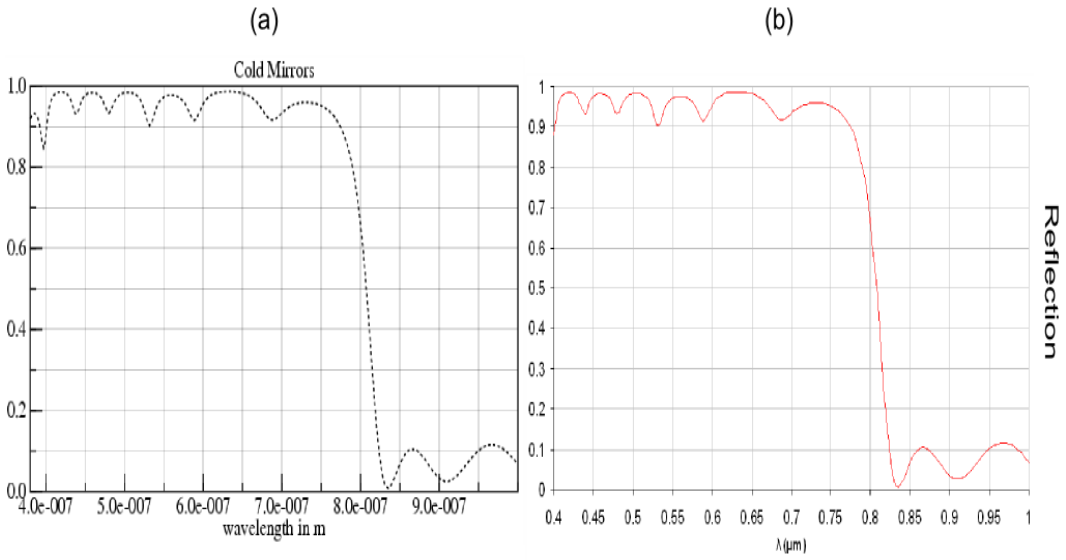


Figure B.2: (a) The results from FreeSnell. (b) The results from the calculation program.

Vita

Jesse Michael Labello was born in Baton Rouge, Louisiana on December 15, 1981 to Donnie Gerald Labello and Marie Louise Schexnayder Labello. He attended Doyle High in his hometown of Livingston, LA until obtaining his diploma in the spring of 2000. He then went to Southeastern Louisiana University for two years where his interest in science was truly initiated. After transferring to Louisiana State University in 2002, he entered a program that allowed him to go to the University of Alabama for the summer of 2003 where he took part in research involving simulation and visualization of synthetic anti-ferromagnets. He graduated from LSU with a Bachelor of Science in physics with a second discipline in electrical engineering in December 2004. Jesse began graduate school in August of 2005 at the University of Tennessee Space Institute in Tullahoma, TN and has performed his graduate research at nearby Arnold Air Force Base since beginning graduate school. Jesse now lives at 411 B.H. Goethert Pkwy, Tullahoma, TN 37388.